Seismotectonics of the thick-skinned Santa Bárbara System in northwestern Argentina: implications for regional crustal rheology and structure

Martin Zeckra[1], Frank Krüger[2], Rodolfo Rodolfo Germán Aranda Viana[3], Fernando Hongn[3], Federico Ibarra[4], Jonathan Weiss[5], and Manfred R. Strecker[2]

[1]Royal Observatory of Belgium
[2]University of Potsdam
[3]Instituto de Bio y Geociencias del NOA
[4]CONICET
[5]NOAA/NWS Pacific Tsunami Warning Center

June 1, 2023

Abstract

The Andean foreland is divided into morphotectonic provinces characterized by diverse deformation styles and seismogenic behavior partially stemming from distinct geological histories that preceded the current phase of subduction. The transition between the high Andes and the eastern foreland is exposed to numerous natural hazards and contains critical economic infrastructure, yet we know relatively little about regional active tectonics due to few geophysical investigations. Here we use waveforms collected during a 15-month-long seismic network deployment in the Santa Bárbara System (SBS) of northwest Argentina following the 2015 Mw 5.7 El Galpón earthquake to determine the distribution and magnitude of local earthquakes, obtain a regional 1D seismic velocity model, and improve our overall understanding of SBS neotectonics. Of the nearly 1200 recorded earthquakes, ~700 occurred in the crust with half of the moment release associated with events deeper than 25 km. The depth extent of seismicity supports the notion that the SBS upper and middle crust are homogeneous and that the lower crust is composed of granulites. These conditions likely formed during Paleozoic mountain building and Salta Rift-related Cretaceous magmatism, which dehydrated the crust. We find no clear indications that a shallow, low-angle detachment fault inferred to have been active during Cretaceous rifting exerts a strong control on modern deformation in contrast to the active décollement beneath the adjacent fold-and-thrust belt of the Subandes to the north. It remains unclear how active, inverted normal faults in the SBS shallow crust connect to the deeper zones of seismicity.

Seismotectonics of the thick-skinned Santa Bárbara System in northwestern Argentina: implications for regional crustal rheology and structure

Martin Zeckra[1,2], Frank Krüger[1], R. Germán Aranda Viana[3], Fernando Hongn[3], Federico Ibarra[1,4], Jonathan R. Weiss[1,5] and Manfred R. Strecker[1]

[1]Institute of Geosciences, University of Potsdam, Karl-Liebknecht-Str. 24-25, 14476 Potsdam-Golm, Germany.

[2]Now at Royal Observatory of Belgium, Avenue Circulaire, 3, BE1180 Brussels, Belgium

[3]Instituto de Bio y Geociencias del NOA, Universidad Nacional de Salta-CONICET, 9 de Julio 14, 4405 Rosario de Lerma, Salta, Argentina,

[4] Instituto Geográfico Nacional, Buenos Aires, Argentina

[5]Now at NOAA/NWS/Pacific Tsunami Warning Center, 1845 Wasp Boulevard, Building 176, Honolulu, Hawaii, 96816, USA

Abstract

The Andean foreland is divided into morphotectonic provinces characterized by diverse deformation styles and seismogenic behavior partially stemming from distinct geological histories that preceded the current phase of subduction. The transition between the high Andes and the eastern foreland is exposed to numerous natural hazards and contains critical economic infrastructure, yet we know relatively little about regional active tectonics due to few geophysical investigations. Here we use waveforms collected during a 15-month-long seismic network deployment in the Santa Bárbara System (SBS) of northwest Argentina following the 2015 M_w 5.7 El Galpón earthquake to determine the distribution and magnitude of local earthquakes, obtain a regional 1D seismic velocity model, and improve our overall understanding of SBS neotectonics. Of the nearly 1200 recorded earthquakes, ~700 occurred in the crust with half of the moment release associated with events deeper than 25 km. The depth extent of seismicity supports the notion that the SBS upper and middle crust are homogeneous and that the lower crust is composed of granulites. These conditions likely formed during Paleozoic mountain building and Salta Rift-related Cretaceous magmatism, which dehydrated the crust. We find no clear indications that a shallow, low-angle detachment fault inferred to have been active during Cretaceous rifting exerts a strong control on modern deformation in contrast to the active décollement beneath the adjacent fold-and-thrust belt of the Subandes to the north. It remains unclear how active, inverted normal faults in the SBS shallow crust connect to the deeper zones of seismicity.

Plain Language Summary

The actively deforming eastern flank of the central Andean plateau in southern Bolivia and northwest Argentina (NWA) contains tectonic structures such as faults that host moderate-sized yet damaging earthquakes in a region with large population centers and critical economic infrastructure. The area is also the youngest part of the longest mountain chain in the word and of particular interest for investigating how mountains grow. However, it remains unclear how north-south variations in the region's geologic history and style of subduction influence modern-day deformation. Here we use the distribution of seismicity recorded after the 2015 M_w 5.7 El Galpón earthquake by a temporary network of seismic instruments to better understand the crustal structure and rheology of the Santa Bárbara System (SBS) in NWA and to address debates regarding the role pre-existing structures play in accommodating active deformation. Our key finding is that most earthquakes occurred in the middle to lower crust extending towards the crust-mantle boundary whereas relatively little seismicity was associated with shallow faults. This finding supports the idea that deep rocks in the SBS are dry due to earlier phases of deformation/magmatism and can support brittle deformation at temperatures normally too high for earthquakes to occur.

Key Points

- Temporary seismic network deployment reveals new details regarding seismotectonics of the thick-skinned Andean foreland in NW Argentina
- Half of the moment release recorded in the seismicity catalog is associated with events deeper than 25 km
- Abundant deep seismicity points to an anhydrous, granulitic lower crust that formed during Cretaceous rifting and magmatism

1. Introduction

The Subandean ranges of southern Bolivia and northwestern Argentina (Figure 1) are associated with wedge-shaped, thin-skinned fold-and-thrust belts that are well-described from geometrical and mechanical perspectives by critical taper theory [e.g., *Dahlen*, 1990; *Dahlen et al.*, 1984; *Davis et al.*, 1983]. Critical taper theory posits that the form of an orogenic wedge is controlled by the mechanical properties of the rocks involved in the deformation, the depth and geometry of a basal décollement, foreland basin geometry, and the ratio between tectonic deformation (i.e., shortening) rate and climatically controlled erosional mass flux [*Willett*, 1999]. When not at steady state, an orogenic wedge can thicken via out-of-sequence deformation on internal structures or widen by foreland-directed lateral growth of the mountain belt, with a well-developed deformation front at the wedge tip, where active thrust faults link with the underlying décollement [*Hilley and Strecker*, 2004; *Weiss et al.*, 2018; *Willett*, 1999].

Southward, the Subandes (SA) transition into the Santa Bárbara System (SBS), which is characterized by uplift of basement-involved uplifted fault blocks, often associated with the inversion of Cretaceous normal faults [*Arnous et al.*, 2020; *Barcelona et al.*, 2014; *Jordan et al.*, 1983; *Kley and Monaldi*, 2002; *Mon and Salfity*, 1995; *Ramos et al.*, 2006]. This thick-skinned style of deformation continues farther south to the Sierras Pampeanas (SP) morphotectonic province, which is characterized by reverse-fault bounded basement blocks [*Jordan et al.*, 1983; *Ramos*, 2000]. In contrast to the SA, the SBS has not developed systematically from west to east and lacks a well-defined frontal deformation zone. Instead, the SBS forms an extensive, tectonically active province with spatially isolated and diachronous uplifts reflected by an unsystematic, fault-controlled river network [*Seagren et al.*, 2022; *Strecker et al.*, 2012].

Major differences between the thin- and thick-skinned sectors of the Andean foreland also exist with respect to geodetically determined, decadal-scale deformation patterns. For example, instead of the steep gradient in horizontal surface velocity documented across the SA [e.g., *Brooks et al.*, 2011; *Weiss et al.*, 2016], GPS data from the thick-skinned sectors including the SBS and adjacent Eastern Cordillera and Andean Plateau morphotectonic provinces display a gradual decrease in horizontal surface velocities from west to east [*Figueroa et al.*, 2021]. This decrease suggests a kinematic style that might be related to either a deep-seated, rheology-controlled décollement, multiple detachment levels, the complete lack of basal low-angle faulting, faulting across isolated and widely distributed steep, basement-cored faults, or a combination of these factors.

Previous work in the SBS and the adjacent Andean interior has greatly improved our understanding of the seismicity and deep structure of the orogen [e.g., *Cahill et al.*, 1992; *Devlin et al.*, 2012; *Mulcahy et al.*, 2014; *Schurr et al.*, 1999; *Schurr et al.*, 2003; *Whitman et al.*, 1992; *Wimpenny et al.*, 2018], but relatively little is known about the active tectonics and seismological characteristics of the upper and middle crust. For example, the suggestion that the broken foreland is part of the SA orogenic wedge and underlain by a shallow, westward-dipping décollement is based solely on structural cross-section balancing [*Grier et al.*, 1991; *Kley and Monaldi*, 2002; *Pearson et al.*, 2013]. Furthermore, although Quaternary deformation in the SBS and adjacent Eastern Cordillera is widespread, the seismogenic nature of faults and associated deformation features is not well established [*Arnous et al.*, 2020; *Barcelona et al.*, 2014; *Figueroa et al.*, 2021; *García et al.*, 2019]. More detailed geophysical information is needed to better characterize the Andean foreland crust, to test structural models that seek to explain the broken foreland deformational style, and to accurately assess regional seismic hazard.

To address this lack of information, we deployed the temporary **STRATEGy** (**S**eismic Ne**T**wo**R**k/**A**rray in Nor**T**hw**E**stern ar**G**entina) seismic network [*Zeckra and Kruger*, 2016] following the October 17, 2015 M_w 5.7 El Galpón earthquake in the southern part of the SBS (Figure 1). Our principal aims were to (1) identify the causative earthquake fault, (2) determine the depth distribution of seismicity, and (3) use the retrieved earthquake data to improve our understanding of deformation patterns in the SBS compared to adjacent morphotectonic provinces. Importantly, the spacing between STRATEGy network stations near the epicenter of the El Galpón event was one tenth of those in the permanent Argentinian national network [*Sánchez et al.*, 2013], enabling us to record elevated aftershock microseismicity and regional background seismicity with a detection threshold two orders of magnitude lower than the regional network. The STRATEGy network was also uniquely positioned above a seismic gap in the underlying subducting Nazca plate and between zones of intermediate- and deep-focus, subduction-related earthquakes (Figure 1) [*Cahill and Isacks*, 1992].

Here, we present results from the STRATEGy seismic network deployment. We describe the semi-automatic post-processing procedure used to generate a local earthquake catalog including hypocenter locations, local magnitudes (*ML*), and focal mechanisms. We also derive a new 1D regional seismic velocity model for the Central Andean foreland crust. The relocated event hypocenters provide new insights into regional crustal structure and rheology and permit a reevaluation of various structural and seismotectonic models proposed for the SBS broken-foreland province and back-arc region in general.

2. Tectonic setting

The SBS is a morphotectonic province located between approximately 23° S and 27° S to the east of the Andean Plateau (known in Argentina as the Puna Plateau), the internally drained high-elevation interior of the orogen, and the abutting thick-skinned thrust belt of the Eastern Cordillera that extends along the eastern border of the Puna Plateau (Figure 1). The SBS is a tectonically active broken foreland [*Jordan et al.*, 1983; *Ramos*, 2000] characterized by diachronous range uplift and deformation [*Alvarado and Ramos*, 2011; *Arnous et al.*, 2020; *Carrera and Muñoz*, 2008; *Hain et al.*, 2011; *Mon and Salfity*, 1995; *Ramos et al.*, 2006; *Strecker et al.*, 2012]. Fault-controlled topography in this region is primarily the result of the contractional Cenozoic inversion of normal faults that formed during Cretaceous extension [*Marquillas et al.*, 2005; *Mon and Salfity*, 1995]. In contrast, in the broken foreland of the Sierras Pampeanas (SP), located between approximately 27° and 33° S [*Jordan et al.*, 1983], shortening is accommodated along deep-rooted reverse faults associated with reactivated Paleozoic basement shear zones, rather than extensional structures [*Bellahsen et al.*, 2016; *Cristallini et al.*, 2004; *Jordan and Allmendinger*, 1986; *Ramos et al.*, 2002].

Although deformation rates in the transition zone between the Eastern Cordillera and the SBS are generally low [*Figueroa et al.*, 2021; *García et al.*, 2019; *McFarland et al.*, 2017], Quaternary fault scarps, folds, and tectonic landforms attest to ongoing activity [*Arnous et al.*, 2020; *Kley and Monaldi*, 2002; *Mon*, 1976; *Mon and Gutiérrez*, 2007] and document sustained, possibly seismogenic, foreland deformation and compartmentalization into smaller sub-basins [*Arnous et al.*, 2020; *Barcelona et al.*, 2014; *Ramos et al.*, 2006]. Strain release in the form of small- to intermediate-size earthquakes also characterize the SBS and adjacent EC [e.g., *Cahill and Isacks*, 1992; *Sánchez et al.*, 2013]. For example, in the past decade, two severe earthquakes resulting in human casualties have occurred in this region: the 2010 M_w 6.3 Salta and the 2015 M_w 5.7 El Galpón earthquakes [*García et al.*, 2013; *Scott et al.*, 2014; *Zeckra*, 2020] (Figure 1). Historical seismicity records further show that this slowly deforming portion of the Andean foreland experiences earthquakes with long recurrence intervals and estimated magnitudes of up to *M* 7 [*Costa et al.*, 2020; *Ortiz et al.*, 2021; *Perucca and Moreiras*, 2009; *Zossi*, 1979]. Despite the regional seismic hazard potential, previous temporary seismic array deployments have focused primarily on large-scale imaging of the boundary between the subducting Nazca and overriding South American plates as well as the investigation of geodynamical processes including those associated with the Puna Plateau [e.g., *Asch et al.*, 2006; *Cahill and Isacks*, 1992; *Laske et al.*, 2013; *Schurr et al.*, 1999; *Whitman*, 1994; *Whitman et al.*, 1992]. Relatively little is known about the seismotectonics of the broken foreland.

3. Data and Methods

3.1 The STRATEGy seismic network deployment

In mid-2016 we installed the temporary STRATEGy seismic network across the SBS, which consisted of 13 seismic stations that recorded earthquake activity for a period of 15 months. The primary aim of the survey was to characterize local and regional seismicity to provide new insight into active tectonics, crustal deformation, and seismic hazard. The network covered a 110 x 58 km area with an average interstation spacing of ~20 km (Figure 2). We focused on areas of potentially recent active faulting based on previous geological, seismological, and geophysical investigations [e.g., *Cahill et al.*, 1992; *Iaffa et al.*, 2013; *Iaffa et al.*, 2011; *Kley and Monaldi*, 2002; *Kley et al.*, 1999; *Whitman et al.*, 1992] in combination with observations from our pilot fieldwork in 2016. We also established our network near the epicenter and in the aftermath of the

2015 M_w 5.7 El Galpón earthquake and the adjacent Cerro Colorado and Sierra de La Candelaria (Figure 2). Three main criteria were considered when determining the locations of the seismic stations: (1) minimizing the depth to bedrock to improve sensor coupling and ensure a wideband signal spectrum, (2) maximizing remoteness as the signal-to-noise ratio is proportional to distance from anthropogenic ambient noise sources, and (3) maximizing security so that seismic stations were preferentially located within sight of nearby settlements to avoid disruptions or security problems.

Each station was equipped with a Lennartz 3D5s seismometer (flat response to ground velocity for frequencies between 0.2 Hz and 50 Hz), except for station 14A, which was equipped with a Mark L-4C-3D short-period sensor. The analog 100 Hz data output was digitized using 23-bit Type 2 DATA-CUBE3 digitizers and stored internally. The power supply came from batteries connected to solar panels. All equipment apart from the solar panels and the external GPS antennas required for accurate time synchronization was buried for protection from heat, insolation, precipitation, and animals. The seismic sensors were buried 0.6 m beneath the surface and oriented towards magnetic north. One exception was station 03B, which was placed in a 2-m-deep concrete vault that formerly housed a regional seismic network site.

A laboratory-based instrument validation test was performed with all seismic sensors prior to the network installation and repeated after dismantling. Based on the input-output cross-spectrum of two sensors with highly correlated signals it is possible to infer the sensors transfer functions [*Havskov and Alguacil*, 2004]. No instrument bias due to alteration of components from previous experiments could be identified. The post-survey tests also ensured instrument parameter consistency during the recording period.

In addition to the data from our network, the Argentinian Seismological Service INPRES (Instituto Nacional de Prevención Sísmica) provided us with continuous waveform data from two permanent seismic network stations [*Sánchez et al.*, 2013] that served to enhance our network coverage (Figure 2). The two stations, separated by 230 km, are located close to the cities of Tucumán (AHML) and Salta (SLA) and are 159 km and 119 km from the El Galpón earthquake epicenter, respectively. Station SLA is equipped with three short-period (nominally 1.0 Hz) Geotech Model S-13 sensors to capture motion in 3 dimensions. A similar vertical-component seismometer exists in Tucumán together with a 3-component Guralp CMG-40 broadband seismometer. Both INPRES permanent stations are equipped with satellite communications, but data transmission was unreliable during the survey period resulting in repeated small gaps in the archived data. Clock synchronization errors also affected the permanent stations; we therefore implemented an automated static time offset correction (STOC) method to identify and correct the associated errors (see Supporting Information S1).

Variable lithology, structural geometry, and subsurface characteristics across our study area affect the appearance of recorded waveforms. Stations 01B, 02A and 05A were located within the Metán Basin (Figure 2), which contains up to 4.5 km of Cenozoic sediments with corresponding alluvial fans in the piedmont of the Sierra de La Candelaria, where unconsolidated sediments rest on the shallow bedrock. Stations 03A and 04A were located on Cretaceous and early Tertiary sedimentary bedrock, respectively. Station 14A was located on steeply dipping, gypsum-bearing lithified strata of marine origin. Despite being located on bedrock within a concrete vault, the waveforms recorded at station 03B show perturbations due to topographic effects because of its elevated position. There are no detailed geological descriptions of the subsurface rheology in the vicinity of stations 06A and 07B.

Several of the stations did not provide continuous recordings over the entire 15-month-long deployment. For example, station 02A recorded for only 158 days before it was stolen. The power supply at station 13A was disrupted by farm animals resulting in a 32-day data gap. Major recording gaps were also associated with high-rainfall conditions during the austral summer months [*Bookhagen and Strecker*, 2008; *Ramezani Ziarani et al.*, 2019; *Strecker et al.*, 2007]. Extreme rainfall events led to complete technical failure for many stations due to corrosion of batteries or charge controllers. The rainfall also limited access to the remote stations and their repair could only be carried out after the monsoon season. Additional information related to network ambient seismic noise levels and associated seasonal variations can be found in the Supporting Information (Figures S1 and S2).

3.2 Seismic Data Processing

Processing and analysis of the seismic data was performed using a semi-automated workflow aimed at minimizing subjectivity while preserving reproducibility and efficacy of statistical uncertainty analysis. We used flexible, open-source python libraries dedicated to seismological data processing including Pyrocko [*Heimann et al.*, 2019], Obspy [*Beyreuther et al.*, 2010], and MTfit [*Pugh and White*, 2018]. We also used QuakeML, an XML-based data exchange standard format for seismology [*Schorlemmer et al.*, 2011], for data storage and to ensure that the entire processing chain associated with the final earthquake catalog could be documented.

3.2.1 Event Detection

Unsupervised event detection is less time consuming than manual scanning of continuous waveform data and preserves a high degree of objectivity in the analysis at the cost of reducing the level of precision. We apply the delay-and-stack method [*Cesca and Grigoli*, 2015; *Grigoli et al.*, 2013], which enables exploitation of the full, continuous waveforms using coincidence information from the whole network. This method is applicable for analyzing a wide range of seismological data associated with processes including volcano-tectonic deformation [*Drew et al.*, 2013; *Langet et al.*, 2014], landslides [*Hibert et al.*, 2014], and induced seismicity [*Comino et al.*, 2017; *Grigoli et al.*, 2013] and is implemented in the Lassie automated full waveform detector [*Comino et al.*, 2017; *Heimann et al.*, 2019]. In the case of the STRATEGy network, the method enables the simultaneous detection of seismic events with a high variability in source-receiver path lengths, focal depths, and waveform characteristics. The unsupervised approach uses arbitrary source locations in a predefined gridded volume (2.5 km cell size) to estimate theoretical arrival times for each station in the network, along which the characteristic functions of the recorded waveforms are stacked. The internal ray-tracer Cake calculates theoretical arrival times for direct P- and S-phases based on a layered-earth model on a spherical Earth. In this step we use the 1D velocity model from the Swiss Seismological Service that was built for a mountainous region and an adjacent foreland basin [*Husen et al.*, 2003] because no comparable velocity model existed for the SBS prior to our study. The application of characteristic functions onto the band-passed waveform data (1 – 15 Hz for P-phases, 1 – 8 Hz for S-phases) removes possible bias due to radiation patterns of the double couple seismic sources and differs for the two seismic phases; STA/LTA (short term average = 1 s, long term average = 8 s) for the sharper P-phase onsets and moving average functions for the more emergent S-phases. The latter induces a strong smoothing, so the resolvability of the source depth vanishes, and the original source volume was reduced to a single horizontal layer at the surface to achieve additional computational efficiency. Finally, the detection trigger is activated after thresholding (threshold = 100) the dimensionless resulting stacked characteristic functions.

3.2.2 Phase picking

Further seismic waveform analysis to estimate event locations and magnitudes depends on accurate identification of seismic phases and their onset times. The list of events detected by Lassie in the previous step provides a robust indicator of time windows within the continuous data stream that contain seismic signals. To accurately determine seismic phase onsets, we use the autoregression phase-picking algorithm implemented in the ObsPy library [*Beyreuther et al.*, 2010] in combination with a coincidence trigger to analyze the identified time windows only at stations that recorded the earthquake. We verified the automatically derived results by manually re-picking events using the dynamic waveform visualization tool Snuffler implemented in Pyrocko (Figure S3). In this step we also assign the polarity of first-motion arrivals for focal mechanism estimation (see section 3.5).

3.2.3 Event location

We use HYPOSAT [*Schweitzer*, 2001] to locate the earthquakes identified in the previous steps based on the arrival times and travel-time differences of direct, reflected, and critically refracted seismic wave phases [*Storchak et al.*, 2003]. A variety of spherical Earth velocity models are available for event location determination but we use AK135 [*Kennett et al.*, 1995], a standard global model for continental regions. Local deviations from this global velocity model within the source region, defined as within a 1.5° radius around the earthquake epicenter, were captured using the CRUST 1.0 model [*Laske et al.*, 2013]. This procedure is largely unsupervised except for the definition of the *a priori* starting depth of 25 km in the HYPOSAT inversion, which is deeper than global averages in continental areas [*Sloan et al.*, 2011] but resulted in more stable and accurate hypocenter estimation in our study area.

3.2.4 Earthquake magnitude estimation

We estimate the magnitudes of earthquakes in our catalog using the updated IASPEI local magnitude (*ML*) scale [*Bormann and Dewey*, 2012]

$$ML = log_{10}A + 1.11log_{10}R + 0.00189R - 2.09 \quad (1)$$

where A is the maximum horizontal trace amplitude measured on a Wood-Anderson instrument and R is the hypocentral distance. The *ML* equation also contains three empirically determined constants, which we derived using the calibration function determined for Southern California that is also used by INPRES [*Sánchez et al.*, 2013] so that our results would be comparable to the national earthquake catalog. The final event magnitude is the mean of all individual station magnitudes calculated using Equation 1 on bandpass (0.1 – 30 Hz) filtered, Wood-Anderson simulated displacement seismograms. As the *ML* value was determined for events with hypocentral distances <1000 km, earthquakes at greater distances were excluded from the fully automated magnitude estimation routine but remain in the catalog with no assigned magnitudes.

3.3 Local 1D velocity model determination

An accurate local seismic velocity model provides a realistic representation of subsurface rheological properties and elastic parameters and helps reduce hypocenter location uncertainties. To derive a 1D velocity model for the SBS we use VELEST [*Kissling et al.*, 1994] and a catalog subset of 215 well-located crustal earthquakes, which we define as events with confirmed P- and S-phase arrivals recorded at a minimum of six stations and with an azimuthal gap smaller than 180°. VELEST solves the coupled hypocenter-model problem by minimizing travel-time residuals using the root-mean-square-misfit. Each step in the inversion yields a solution consisting of an earthquake hypocenter, station corrections, and a 1D velocity model. VELEST inverts for layer velocities only and not for layer thicknesses or the number of layers. Therefore, we use a trial-and-error approach to determine the best layered model set-up for the P-wave velocity only, since this component is subject to lower uncertainties and yields more stable solutions. We arrive at our preferred model by performing stability tests that include varying the initial hypocenter location (random, by 5 and 10 km), resampling the catalog (20, 50, 100 events randomly omitted), and creating geographical subsets that broadly correspond to variations in local geology. These tests permit exploration of weighting schemes for different layers and help stabilize the inversion for layers crossed by a small number of ray paths (e.g., at mantle depths or in the shallow sedimentary layer). The final velocity model (see Section 4.2; Table 1; Figure 5) is constructed from layer-wise averaging of the best 10% of 5000 model runs. We simultaneously invert for P- and S-wave velocities and calculate V_P/V_S ratios from the individual model outcomes. We down-weight S-wave arrival times by 50% and dampen the respective station correction by a factor of 2.0 in contrast to a factor of 0.1 for the P-wave station corrections. This scaling accounts for the greater uncertainties associated with the emergent character of the S-wave arrivals. VELEST hypocenter solutions deviate from the starting locations by a few kilometers at most so we chose not to use them to update the event catalog.

3.4 Double-difference relocation

A major challenge to using seismological data to derive a high-resolution image of seismotectonic structures and processes is large hypocenter location uncertainties. As mentioned earlier, refining the local velocity model helps reduce the absolute location errors of well-defined hypocenters. Location accuracy can be further improved using inter-event travel-time differences. We use the joint hypocenter determination method implemented in HypoDD [*Waldhauser and Ellsworth*, 2000], which simultaneously minimizes the travel time difference uncertainty of two linked events located <12 km apart observed at two seismic stations (i.e., double-differencing) across the catalog of 8,371 event pair combinations. The inclusion of >3,000 cross-correlation differential phase arrival times further increases the location accuracy of 408 events.

3.5 Focal mechanism determination

In addition to providing a basis for rigorous analysis of tectonic structures based on the spatial distribution of precisely located earthquakes, the first-motion polarity from single earthquake sources can be used to invert for earthquake focal mechanisms. We use MTfit [*Pugh and White*, 2018], which employs Bayesian inversion scheme to estimate the most likely source model in the form of marginal probability density functions of the observation parameters (e.g., polarity and amplitude). A Monte Carlo random sampling draws 2.5 million moment tensor solutions per event that are reduced to three independent parameters (strike, dip, rake) by normalizing the moment tensor and assuming double couple point sources for the pure tectonically induced microseismicity [*Pugh et al.*, 2016]. Source–receiver paths are constructed from azimuth and incidence angles using the Cake ray-tracer tool [*Heimann et al.*, 2019], the high-precision HypoDD locations, and our new 1D seismic velocity model. Out of 208 earthquakes with an azimuthal gap <180º we obtained 22 reliable focal mechanisms (Figure 4; Table S1).

4. Results

4.1 Seismicity Catalog

The earthquake catalog derived from the STRATEGy network deployment consists of 1919 automatically detected events throughout the 15-month recording period, resulting in an average of ~4.3 events/day. However, due to heavy rainfall events, daily recorded seismicity was inconsistent during the austral summer, resulting in a temporary decrease in the number of operational stations and fewer recorded earthquakes (Figures S4 and S5). During the first five months of recording with a full network, an average of 10±5 events/day was detected. This rate gradually decreased over time until 0 events/day were recorded towards the end of the monsoon season, when only three stations were operational. The time-dependent event decay rate based on Omori's law [*Utsu et al.*, 1995] suggests that some of the events recorded early in the survey were aftershocks of the 2015 M_w 5.7 El Galpón earthquake (see Supporting Information S2). Following restoration of the damaged stations, the event-detection rate remained stable at three events/day during the last four months of recording, presumably reflecting the background seismicity rate. This value is higher than previous estimates not only for this area [*Cahill et al.*, 1992], but also for continental intraplate environments such as western Anatolia [*Akyol et al.*, 2006] and parts of Central Asia [*Schurr et al.*, 2014; *Sippl et al.*, 2013], and is closer to values found near active plate boundaries such as New Zealand and the Himalayas [*Michailos et al.*, 2019; *Monsalve et al.*, 2006].

We determined the hypocenter locations and *ML* for 1435 earthquakes. After excluding 236 events with a fixed depth, we generated a refined catalog of 1199 earthquakes with assigned hypocenter uncertainties. We then categorized earthquakes with local (<100 km) to regional (<1000 km) epicentral distances into three distinct groups: (1) shallow crustal earthquakes at depths <50 km, (2) intermediate-depth earthquakes within the Wadati-Benioff Zone at a depth of ~200 km, and (3) deep earthquakes located at depths >500 km (Figures 1, 2, and S6).

Of the latter, earthquakes with a hypocentral depth of ~600 km align along a narrow band striking nearly north-south located to the east of the orogen (Figure 1). The largest magnitude, non-teleseismic event in our catalog falls into this category (date: 20170221; origin time: 14:09:07.7 UTC; depth: 646 km; *ML* 7.3; M_W 6.5). Intraslab activity within the Wadati-Benioff zone of the subducting Nazca Plate is restricted to the northwest corner of our network beneath the Andean Plateau. This area of seismic activity has previously been referred to as the “Jujuy Nest" [*Cahill and Isacks*, 1992; *Kirby et al.*, 1996; *Mulcahy et al.*, 2014; *Valenzuela-Malebrán et al.*, 2022] (Figure 1) and is thought to be associated with dehydration of the subducting plate and the partial melting of the overlying asthenospheric wedge [*Kirby et al.*, 1996; *Schurr et al.*, 2003]. Crustal earthquakes with *ML* 0.5-4.6 are confined to the Eastern Cordillera and the Central Andean foreland. Recorded seismic activity diminishes northward towards the SA but broadens to the south toward the SP. Importantly, the earthquake hypocenters are distributed over the entire thickness of the crust down to the approximate depth of the Moho at 43 km [*Laske et al.*, 2013; *Tassara and Echaurren*, 2012] (See Section 4.3 and Figures 4 and 5).

Absolute hypocenter-location uncertainties, which we estimated while inverting for the source locations, are primarily related to source-receiver distances. Epicentral location errors are less than 10 km for events within 30 km of the network (Figure 3) and increase to tens of kilometers at regional distances <1000 km. Our estimates of focal-depth uncertainty for crustal earthquakes are limited to events within the STRATEGy network with azimuthal coverage <180°. Large uncertainties around station AHML reflect time-synchronization errors. The application of double-difference relocation for 408 local earthquakes within the network lowered their theoretical location uncertainty by a factor of 1000 compared to the primary hypocenter estimations resulting in a median horizontal uncertainty of 2.8 m with 99% of the location uncertainties smaller than 10 m.

We obtained a magnitude of completeness (M_C) for the investigated area of 1.45 using the b-value stability approach [*Woessner and Wiemer*, 2005]. Separating local and regional crustal events yields M_C values of 1.3 and 2.1, respectively. The M_C values of 2.6 and 3.6 for intermediate-depth and deep-focus events are below the INPRES catalog M_C of 3.9 for events in the study area over the same time. The overall detection limit (minimum observable magnitude) increases linearly with hypocentral distances >45 km and by one earthquake magnitude for every 303 km increase in hypocentral distance. Station magnitude residuals follow normal distributions (Figure S7) with mean values reflecting station site characteristics and shallow subsurface lithology. For example, positive residuals are related to amplification effects within the intermontane Metán Basin due to the thick layer of unconsolidated sediments, whereas negative residuals are associated with stations located on or close to bedrock.

Recorded earthquakes at mid- to lower-crustal depths (~25-40 km) are widely scattered throughout the study area (Figures 2 and 4). The base of the zone of lower-crustal seismicity is sub-horizontal and dips gently northwestward, reaching depths close to the Moho beneath the Eastern Cordillera (Figure 4). Earthquakes located at depths greater than ~25 km are responsible for approximately half of the moment release during the observation period (Figure 5). This is consistent with the relatively low b-value of 0.75 calculated from the earthquake magnitude-frequency distribution and the suggestion that deeper hypocenters tend to be associated with larger magnitude events [*Amitrano*, 2003; *Mori and Abercrombie*, 1997].

The upper crust at depths shallower than ~25 km appears to be mostly aseismic across the Eastern Cordillera-Santa Bárbara System transition (i.e., beneath the Sierra de Metán in the northern SBS and the Sierra del Brete and the Choromoro Basin in the southern SBS; Figure 3). Moving eastward towards the foreland, however, shallow, low-magnitude earthquakes are most likely associated with upper crustal structures in the Metán Basin, beneath the Cerro Colorado as well as beneath and north of the Sierra de La Candelaria (Figure 4b and c). This shallow seismicity transitions with increasing depth to pronounced zones of earthquake activity concentrated around the M_w *5.7* El Galpón and *ML* 5.3 Rosario de la Frontera earthquake hypocenters (Figures 2 and 4). These events occurred prior to the installation of our temporary network and many of the recorded earthquakes are likely aftershocks (see below). The first cluster is in the north in the vicinity of the 2015 M_w 5.7 El Galpón event, and the aftershocks appear to occur along one of the suggested fault plane solutions, aligning nearly north-south and extending over a wide depth range roughly coincident with a steep, east-dipping fault plane. Aftershocks extend down to a depth of ~30 km, which is generally deeper than global continental averages for teleseismically-determined earthquake focal depths [e.g., *Sloan et al.*, 2011]. The second cluster is likely associated with the *ML* 5.3 earthquake that occurred on September 5, 2015, approximately 47 km south of the El Galpón earthquake epicenter. The location uncertainties associated with this cluster are too high to definitively relate it to any seismotectonic structures, and the distribution recorded with the temporary network supports both N-S- or E-W-striking fault orientations. The absence of moment-tensor solutions for the *ML* 5.3 event prevents any further first-order source characterization due to its small magnitude. Overall, mid- to lower-crustal seismicity is more diffuse in the southern portion of the SBS than in the north.

4.2 Regional distribution of events

The Metán Basin appears to play an important role in controlling both the along-strike structural segmentation of the SBS [*Kley and Monaldi*, 2002] and the observed seismicity (Figures 2 and 4). South of the basin, Proterozoic metamorphic basement rocks are exposed at the surface, forming the nucleus of the Sierra de La Candelaria, for example, and only a few reverse faults cut the crust. In contrast, the exposed strata north of the basin are generally younger and primarily west-verging faults outcrop at the surface. There are also subtle, but distinct differences in the spatial distribution of earthquake hypocenters, although our dataset captures seismicity primarily surrounding and to the south of the Metán Basin with some deeper events extending to the north (Figures 1 and 2). Shallow seismicity essentially terminates just north of the Garrapatas transfer zone and in map view the hypocenters concentrate around the edges and particularly to the east of both the Metán and Choromoro Basins (Figure 2). Seismicity generally shallows approaching the eastern edges of these basins, with deeper events located beneath the central Metán Basin, the Sierras de Metán and La Candelaria. More abundant seismicity characterizes the crust beneath the Metán Basin and the Cerro Colorado range, particularly at mid-crustal depths where a broad peak in the depth distribution of seismicity centered at ~18 km is observed (Figure 5). The largest cluster of events is found beneath the surface trace of the Metán Basin Central Thrust Fault [MBCTF; *Iaffa et al.*, 2011] and is likely associated with the aftershock sequence of the El Galpón earthquake. Seismicity is far less abundant beneath Sierra de La Candelaria, and there is no distinct peak in the depth distribution of the events; earthquake hypocenters are evenly distributed throughout the crust to a depth of ~30 km (Figure 5).

4.3 1D velocity model

Our final 1D velocity model (Table 1; Figure 5) consists of five layers including two shallow sedimentary layers, an upper and lower crust, and the upper mantle. We divide the shallow sediments into upper, unconsolidated, and lower, compacted layers, which are resolvable based on contrasting P-wave velocities and a significant difference in the V_P/V_S ratio. The lack of crossing ray paths associated with deeper-than-average focal depths likely results in greater velocity uncertainties in the shallow sediments compared to the other layers. For the shallow sediments, rock properties such as porosity, pore-fluid pressure, and strength influence seismic velocity [*Lee*, 2003]. Previously recognized regional lithological variations [*Iaffa et al.*, 2011] are reflected in the station velocity residuals of the stations compared to average subsurface velocities. For example, station 05A located in the center of the sediment-filled Metán Basin yields very high S-wave residuals of ~1.4 seconds. The S-wave velocities in the shallow layers are better constrained than the P-wave velocities. Hence, the large V_P/V_S ratio uncertainties are primarily due to the V_P estimates. Our results confirm the presence of strong lateral and vertical lithological heterogeneities in the shallow subsurface (i.e., unconsolidated basin fill on top of and adjacent to fault-bounded, metamorphic basement rock) throughout the study area.

The upper crust of the SBS, in contrast, is largely homogeneous and characterized by constant velocity between the depths of 4 and 33 km. The upper crustal V_P/V_S ratio of 1.76 is close to the value obtained using our dataset and a Wadati diagram [*Zeckra*, 2020] (Figure S8). A substantial increase in V_S at a depth of 33 km and an associated reduction in V_P/V_S to an abnormally low value [*Christensen*, 1996] characterizes the transition from the upper to the lower crust. Additional variations in the seismic velocities of the SBS crust cannot be ruled out, but additional rheological information (e.g., temperature, heat flux, stress, density) is required to resolve finer details (Figure 4).

The Moho is delineated by an increase in V_P, V_S, and V_P/V_S at a depth of 43 km, which is an approximate depth since only a few ray paths penetrate the crust-mantle boundary. The low uncertainty beneath this depth results from strong damping of the mantle velocity variations in the inversion bounded by values from tomographic studies and global velocity models [*Laske et al.*, 2013] as only a few ray paths penetrate the crust-mantle boundary.

At shallow crustal levels our new velocity model compares favorably with global models such as AK135 and CRUST1.0 [*Kennett et al.*, 1995; *Laske et al.*, 2013]. With increasing depth, however, our inverted velocity values are generally lower and the layer boundaries deeper than the global estimates. For example, the Moho is situated 2.6 and 8 km deeper than the CRUST1.0 and AK135 models, respectively. We suggest that our 1D model provides an enhanced regional picture of the crust and upper-mantle velocity compared to the global estimates.

5. Discussion

5.1 Proposed crustal fault geometries versus broken foreland seismicity

Three decades ago *Grier et al.* [1991] suggested that compressional inversion and reactivation of Cretaceous Salta Rift extensional structures including shallow (listric) normal faults and a basal sub-horizontal shear zone representing the brittle-ductile transition (i.e., the principal detachment) at a depth of 10-12 km exerts a primary control on foreland basin and fault geometries during Cenozoic contractional Andean orogenesis. Subsequent studies [e.g., *Cahill et al.*, 1992; *Cristallini et al.*, 1997; *Iaffa et al.*, 2011; *Kley and Monaldi*, 2002] generally support this interpretation with proposed modifications of the detachment level and number of detachments. While reactivation of inherited basement heterogeneities is generally accepted as an important mechanism during the tectonic evolution of basement-uplift provinces, the link between the activity of surface structures and motion along deep-seated crustal heterogeneities is the subject of ongoing debate [e.g., *Ammirati et al.*, 2022; *Bellahsen et al.*, 2016; *Brooks et al.*, 2003; *Lacombe and Bellahsen*, 2016; *Ramos et al.*, 2004].

In the SBS there is structural evidence for reactivation and inversion of normal faults [e.g., *Abascal*, 2005; *Cristallini et al.*, 1997; *Iaffa et al.*, 2013; *Iaffa et al.*, 2011; *Kley and Monaldi*, 2002; *Kley et al.*, 1999; *Kley et al.*, 2005; *Mon and Salfity*, 1995] but the distribution of crustal earthquakes recorded during our network deployment is only partially compatible with these observations. At depths ≤10 km, sparse earthquake hypocenters lie in the vicinity of a closely spaced series of reverse and inverted normal faults beneath the Cerro Colorado and the Metán Basin (Figure 4). A few shallow earthquakes also occurred beneath the Sierra de la Candelaria and in close proximity to the surface trace the MBCTF [*Iaffa et al.*, 2011], which may have hosted the 2015 M_w 5.7 El Galpón earthquake; a down-dip extrapolation of the steep, near-surface portion of the MBCTF passes through the El Galpón hypocenter. However, most relocated shallow events do not cluster along continuous planes that coincide with the location of shallow faults, nor can the earthquakes be easily projected from the surface to deeper depths (Figure 4).

Structural cross sections tend to place the base of recently active faults at ~15 km where they are interpreted to intersect the low-angle detachment horizon even though the maximum penetration depth of regional seismic reflection data is ~8 km [e.g., *Iaffa et al.*, 2011]. There is a distinct peak in the relocated seismicity depth distribution histogram at ~12 km (Figure 5) but in cross-section only a few events coincide with the inferred location of the detachment (e.g., directly beneath the MBCTF and beneath and to the east of the Sierra de la Candelaria; Figure 4) suggested by *Grier et al.* [1991]. Thus, the proposed connection between the low-angle shear zone that facilitated Cretaceous extension and present-day seismicity is unclear. This apparent disconnect is in line with recent numerical modeling results that suggest pure-shear, thick-skinned deformation is required to explain the structural evolution of the SBS [*Liu et al.*, 2022] in contrast to the simple shear, detachment-involved, thin-skinned tectonics that characterize the SA. Furthermore, a recent reevaluation of the GPS-derived, horizontal surface velocity field [*Figueroa et al.*, 2021] questions the notion that a shallow décollement beneath the SBS controls deformation [e.g., *McFarland et al.*, 2017] and instead suggests that structures such as a much deeper, rheology-controlled décollement, multiple detachment levels or the complete lack of basal low-angle faulting and faulting across isolated and widely distributed steep basement faults, or a combination of these factors are more likely. If the inherited rift-related structures and a basal detachment control SBS contractional deformation, we would expect a clearer link between these features and the relocated earthquakes at shallow and/or mid- to lower-crustal depths.

The lack of correspondence may be partially due to the limited duration of our seismic network deployment. Most crustal earthquakes recorded in our study occur around the 2015 epicenters and near the eastern limits of the SBS despite the lack of a well-defined deformation front and elongate thrust fault-related structures (Figure 2). We suspect that the map-view seismicity pattern is a transient feature characteristic of active broken-foreland provinces, where localized deformation on reverse faults that are short in map view increases stress-loading on adjacent structures until they fail, resulting in non-systematic patterns of deformation [e.g., *Hilley et al.*, 2005]. A similar deformation style, with spatially separate and diachronous reverse-fault bounded range uplifts, has been ascribed to the Cretaceous Laramide province of North America [*Marshak et al.*, 2000] and the Cenozoic Tien Shan of Central Asia [*Burbank et al.*, 1999; *Liu et al.*, 2022]. Future regional seismic deployments would likely capture different earthquake spatial patterns including events that might align more closely with some of the shallow structures. However, the correspondence between the distribution of Cretaceous rift-related sediments and the earthquake hypocenters (Figures 1 and 2) points to inherited rheological control [e.g., *Wimpenny*, 2022].

5.2 Implications for crustal composition and structure of the SBS

The earthquake hypocenter distribution involves nearly the full extent of the continental crust (Figures 4 and 5), which has significant implications for the overall crustal structure and rheology of this portion of the orogen. The base of seismicity terminates abruptly in the lower crust and dips gently westward; the deepest relocated events are located ~10 km above the Moho in the eastern SBS and are at or slightly above the Moho approaching the Eastern Cordillera in the west (Figure 4). The general lack of deeper hypocenters suggests the presence of a boundary akin to a brittle-ductile transition just above the Moho.

The homogeneous seismic velocity within the upper crust (Figure 5) indicates low heat flow comparable to cratonic environments [*Currie and Hyndman*, 2006]. This characteristic might be partially explained by underthrusting of the old and cold Brazilian Shield, which has been related to the large degree of SA shortening [*Allmendinger and Gubbels*, 1996; *Babeyko and Sobolev*, 2005; *Gubbels et al.*, 1993; *Kley et al.*, 1996; *Lamb*, 2000; *Liu et al.*, 2022], although there are no unambiguous indications that this process influences SBS deformation. The 1D seismic velocities also suggest the existence of a felsic mid-crustal layer with lower than global average velocities [*Christensen and Mooney*, 1995]. This interpretation is compatible with recently published thermal, strength, and rheological models [*Ibarra et al.*, 2019; *Ibarra et al.*, 2021] in addition to well logs from the La Candelaria region [*Arnous et al.*, 2020].

Seismicity that extends across the entire crust implies brittle deformation at temperatures as high as ~600º C [Figure 5; *Sloan et al.*, 2011], which contrasts the standard view of crustal seismicity, where the quartzo-feldspathic lower crust is hydrous, weak, and aseismic beneath a shallow, temperature-controlled, brittle-ductile (i.e., seismic-aseismic) transition at 300-350ºC [*Maggi et al.*, 2000; *Scholz*, 1998; *Sibson*, 1982]. Deep seismicity at elevated temperatures is related to an anhydrous lower crust [*Jackson et al.*, 2004; *Yardley and Valley*, 1997]. Such environments are typically associated with partial melting of granites, related magmatism at temperatures of ~700º C, and the formation of metastable mafic granulites, which remain strong and brittle at elevated temperatures [e.g., *Jackson et al.*, 2008; *Jackson et al.*, 2004; *Maggi et al.*, 2000]. Examples of such environments are the Himalayan collision zone, where the Indian Shield is underthrusting Tibet [e.g., *Copley et al.*, 2011; *Craig et al.*, 2012], and the southern East African Rift System (EARS), where rift-related magmatic dehydration of the lower crust and associated changes in lower crustal composition that support deep brittle deformation have been inferred [*Craig and Jackson*, 2021; *Jackson et al.*, 2008; *Maggi et al.*, 2000].

The regional temperature and stress conditions that promote deep brittle deformation beneath the SBS are best explained in the context of Mesozoic extensional tectonism and magmatism that generated an anhydrous lower crust (i.e., similar to portions of the modern-day EARS) and the subsequent evolution toward contractional tectonics during Cenozoic Andean orogenesis. The rheological properties and geological history of the SBS are markedly different than the seismically quiet, thin-skinned SA. The conditions that drive SBS deformation are more akin to the thick-skinned SP to the south where seismicity occurs along fault planes that extend across the entire crust and are believed to be reactivated crustal heterogeneities including Proterozoic or Early Paleozoic sutures and/or Late Paleozoic or Mesozoic graben normal faults. The seismicity ceases where the structures are inferred to intersect a shear zone at or slightly above the Moho that may represent the main Andean décollement, which facilitates the eastward transfer of Andean shortening to the SP [*Bellahsen et al.*, 2016; *Lacombe and Bellahsen*, 2016; *Ramos*, 1988; *Ramos et al.*, 2002; *Smalley Jr. et al.*, 1993]. It is worth noting that there is also evidence in the SP for regional granulite facies metamorphism related to Paleozoic orogenesis and a resulting anhydrous lower crust [*Rapela et al.*, 2010; *Wimpenny*, 2022].

The notion that the SBS lower crust is compositionally unique and anhydrous is supported by the presence of granulite xenoliths of granitic and mafic composition retrieved from dikes and sills intruded into the Cretaceous syn-rift sediments of the Salta Rift at about 90 Ma [*Galliski and Viramonte*, 1988; *Gioncada et al.*, 2010; *Lucassen et al.*, 1999; *Viramonte et al.*, 1999]. Granulite-xenolith thermobarometry suggests equilibration temperatures of 850-900°C and pressures that correspond to a depth of ~35 km [*Lucassen et al.*, 1999]. The petrologic evidence documents contemporaneous mafic volcanism and granulite-facies metamorphism in the realm of the Salta Rift at depths >30 km during Cretaceous extension. Although mafic granulites account for only ~5% of all known granulitic xenoliths [*Lucassen et al.*, 2007; *Lucassen et al.*, 2005; *Lucassen et al.*, 1999] and the total addition of mafic melts to the crust may be limited [*Franz et al.*, 2006], large portions of the lower crust beneath the Salta paleo-rift are likely mafic. The portions of the SBS that were affected by Cretaceous melting or metamorphism-related depletion of hydrous minerals now host deep brittle deformation. These conditions may even apply to areas where volcanism was not dominant and where limited extensional faulting was only associated with coeval deep-seated emplacement of magmatic dikes and sills, as suggested by observations from other regions [e.g., *Behn et al.*, 2006; *Buck et al.*, 2005; *Tongue et al.*, 1992; Figure 6].

Estimates of the local yield strength envelope (YSE) indicate that the SBS lower crust is strong, and that the brittle-ductile transition zone is located close to the Moho [*Ibarra et al.*, 2019; *Wimpenny*, 2022] (Figures 4 and 5). The YSE shown in Figure 5c represents our preferred scenario based on published regional thermal and density models [*Ibarra et al.*, 2019; *Ibarra et al.*, 2021], our new velocity model (i.e., the anomalous lower crust V_P/V_S ratio), the associated inferred rheology, and corresponding published values for coefficients of friction [e.g., *Christensen*, 1996; *Christensen and Mooney*, 1995; *Zoback et al.*, 1987]. More specifically, the YSE was calculated by assuming that the upper crust is composed of quartz diorite, the lower crust is granulitic based on xenolith composition and lower-than-average seismic velocities, and the coefficient of friction is 0.1 based on the assumed presence of inherited crustal structures. This combination of model parameters places the brittle-ductile-transition at a depth of ~38 km, which is consistent with the depth distribution of recorded hypocenters but deeper than recent geodynamical models that show high strain accumulation at the top of the lower crust and a broad deformation zone extending into the mid-crust beneath the shallow faults [e.g., *Liu et al.*, 2022; Figure 6]. Our strength profile is also in line with results stemming from a recent examination of the relationship between the distribution of Mesozoic rifts and seismicity along the length of the Andean foreland, which suggests low effective coefficients of friction and the presence of granulites in the lower crust to explain the deep seismicity in locations where ancient rift basins exist [*Wimpenny*, 2022].

Elevated thermal gradients established during Cretaceous rifting, associated melting, magmatism, and the formation of an anhydrous lower crust contrast sharply with the adjacent SA, where no extensional processes have influenced the rheological properties of the crust. The deep crustal earthquakes in the SBS are best explained by thermally controlled lithological and compositional changes, as well as inherited structures, associated with Cretaceous rift-related magmatic processes that caused an overall embrittlement of the lower crust. In this context it is interesting to note that similar observations have been reported from the southeastern Colombian Andes, which experienced lower crustal dehydration due to rifting and magmatism prior to Cenozoic Andean mountain building [*Vásquez and Altenberger*, 2005; *Weber et al.*, 2002]. Evidence of these processes include mafic granulitic xenoliths retrieved from Cenozoic volcanic rocks in the region, which is currently seismically active to depths of ~40 km [*Monsalve et al.*, 2019; *Taboada et al.*, 2000; *Wimpenny*, 2022].

5.3 A revised seismotectonic model for the SBS

Our temporary seismic network deployment installed after the 2015 El Galpón earthquake recorded abundant seismicity throughout the SBS crust. The resulting hypocenter distribution suggests the presence of two distinct zones of seismicity. Approximately one third of the recorded events occurred above a depth of ~20 km, in the general vicinity of steeply dipping faults, some of which are reactivated and inverted normal faults (Figure 4). The most likely interpretation is that Andean contractional deformation has reactivated the shallow basement heterogeneities/anisotropies and inverted some of the upper crustal faults. The widespread distribution of both recently active structures and seismicity in the foreland supports this view. Existing structural models suggest that the shallow faults root in a décollement that is similar in depth and related to the low-angle detachment fault that was active during Cretaceous extension when the Salta Rift sediments were deposited in different depocenters (Figure 1). However, our new seismicity observations in combination with the recent numerical modeling and geodetic results [*Figueroa et al.*, 2021; *Liu et al.*, 2022], suggest that the low-angle detachment fault does not play a decisive role in controlling compressional deformation in the SBS. The limited shallow seismicity agrees with modeling results that show minor strain accumulation in the vicinity of the shallow/inverted normal faults [e.g., *Liu et al.*, 2022; Figure 6]. The details of the relationship between the active/seismogenic shallow structures and the extension-related detachment fault remains unclear (Figure 6).

The remainder of the recorded seismicity occurred in the middle and lower crust. At depth, hypocenters terminate abruptly above the Moho across a sharp, sub-horizonal boundary that dips gently northwestward towards the Eastern Cordillera. Mid- and lower-crustal seismicity in the SBS is diffuse and does not delineate individual through-going structures.

Petrological data including the widespread distribution of mafic, granulite xenoliths indicate very dry conditions at depths of several tens of kilometers. Thus, the SBS lower crust is anhydrous and has experienced high-temperature metamorphism. These characteristics allow for the broad distribution of present-day deep seismicity. The upper and middle crust comprise one homogeneous layer extending down to a depth of ~33 km and likely consist of quartz diorite, while the lower crust is composed of metastable and dry mafic granulites. Low heat flow and low friction coefficients push the brittle-ductile transition zone to a depth of ~38 km.

6. Conclusions

We present a view of Andean foreland seismotectonics based on earthquakes recorded during a 15-month network deployment across the thick-skinned Santa Barbara System of Northwestern Argentina in the aftermath of the 2015 M_w 5.7 El Galpón earthquake. Regional seismicity falls into 3 general categories including shallow crustal events at depths <50 km, intermediate-depth earthquakes at ~200 km related to subduction of the Nazca Plate beneath the Andes, and deep earthquakes located at depths >500 km. We focus our attention on the crustal earthquakes and find that brittle deformation is confined primarily to the easternmost, low-relief portion of the Andean foreland. A double-difference relocation of the shallow microseismicity hints at activity along steep reverse faults, many of which are reactivated structures formed during Cretaceous extension and creation of the Salta Rift. The earthquake hypocenters extend to the Moho at a depth of ~40 km before terminating in a sub-horizontal zone that is shallow in the east beneath the range-front faults and deepens gradually westward approaching the high-topography Eastern Cordillera and Puna Plateau. Half of the moment-release in the catalog is associated with earthquakes below 25 km. The deep extension of the seismogenic zone and broadly distributed brittle deformation in the lower crust does not clearly delineate distinct structures extending from shallow depths. The observed homogeneous crustal composition inferred from modeled seismic velocities, unusually low V_P/V_S ratios, and petrologic evidence of granulite-facies rocks in the lower crust are consistent with Cretaceous rifting and associated magmatism that resulted in highly fractured, anhydrous conditions that promote deep seismogenesis. The transition from the adjacent, seismically quiet Subandean ranges in the north to the highly seismogenic Santa Barbara System is abrupt and associated with the distribution of Salta Rift related structures and associated magmatism. Map-view seismicity broadens southward crossing into the Sierras Pampeanas and associated large, range-bounding faults. The results from our local seismic network deployment help fill a gap in knowledge related to the seismogenic thickness of the Andean lithosphere and shed new light on the seismotectonics of an actively deforming broken foreland strongly influenced by the regional tectonic history.

Acknowledgments

The research was supported within the framework of the project IGK 2018 SuRfAce processes, Tectonics and Georesources: The Andean foreland basin of Argentina (StRATEGy) and funded by the Deutsche Forschungsgemeinschaft (DFG, grant to M.R. Strecker and F. Krüger STR 373/34-1) and the Brandenburg Ministry of Sciences, Research and Cultural Affairs, Germany. Field visits were furthermore supported by a Centro Universitario Argentino-Alemán grant (CUAA/DAHZ) by the German Academic Exchange Service (DAAD) to M.R.S. We thank the University of Potsdam for providing the seismic instrumentation and INPRES for providing access to waveform data for two of their stations. We also thank Municipalidad de El Galpón and

Instituto de Bio Y Geociencias del NOA (Conicet-UNSa) for logistical support. The earthquake data from this study can be accessed through the ISC Seismological Dataset Repository at https://doi.org/10.31905/YTIR1IED. The Generic Mapping Tools [GMT; *Wessel et al.*, 2013] was used to create the figures presented in this paper.

layer	depth [km]	v_P [km/s]	v_S [km/s]	v_P/v_S
unconsolidated sediments	-3.0	4.16 ± 0.60	2.83 ± 0.11	1.45 ± 0.17
compacted sediments	1.5	5.71 ± 0.22	2.83 ± 0.11	2.02 ± 0.13
upper crust	4.0	5.81 ± 0.05	3.30 ± 0.04	1.76 ± 0.01
lower crust	33.0	6.65 ± 0.31	4.33 ± 0.08	1.54 ± 0.05
mantle	43.0	8.04 ± 0.07	4.49 ± 0.04	1.79 ± 0.02

Table 1 Final minimum 1D velocity model. Velocities estimated from the median and standard deviations of stable solutions at each layer from a uniform variety of starting models and manually defined layer depths by merging layers of homogeneous velocities in initial, fine-grid test models.

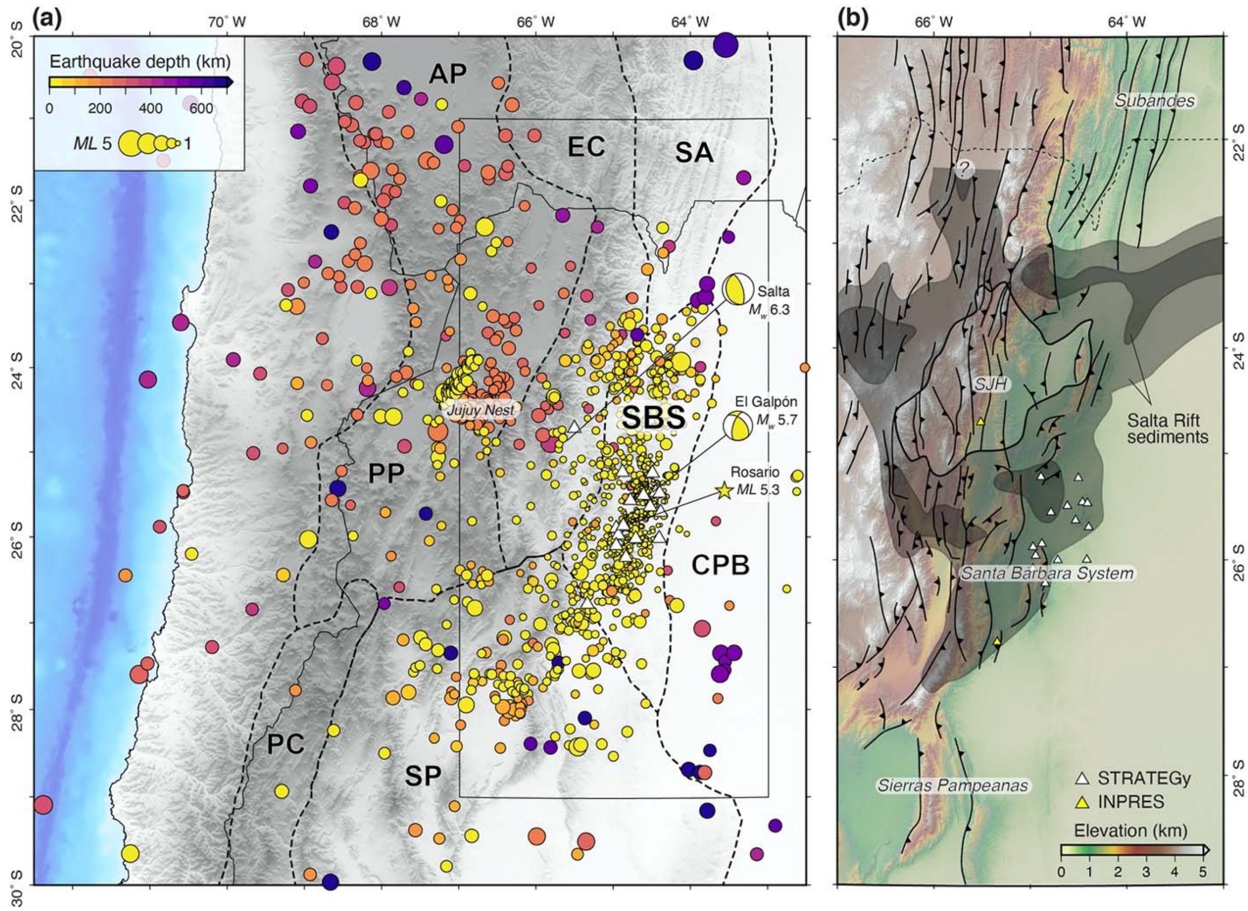

Figure 1 Seismicity and regional physiographic/tectonic structures. (a) All earthquakes recorded during the 15-month-long network deployment, color-coded by depth, and scaled to estimated local magnitudes (*ML*). Also shown is the location of the seismic network (white triangles) and the USGS focal mechanism for the 2015 El Galpón earthquake. (b) Close-up view of Cenozoic structures [*Casa et al.*, 2014; *Kley et al.*, 2005; *Mon and Salfity*, 1995; *Pingel et al.*, 2013]. Extent of the Cretaceous Salta Rift from *Kley et al.* [2005] with dark gray shading representing rift-related sediment thicknesses greater than 2000 m. White triangles are STRATEGy station locations; yellow triangles denote INPRES stations referred to in the main text. AP=Altiplano; PP=Puna Plateau; EC=Eastern Cordillera; SA=Subandes; SBS=Santa Bárbara System; SP=Sierras Pampeanas; CPB=Chaco-Paraná Basin; SJH=Salta-Jujuy High.

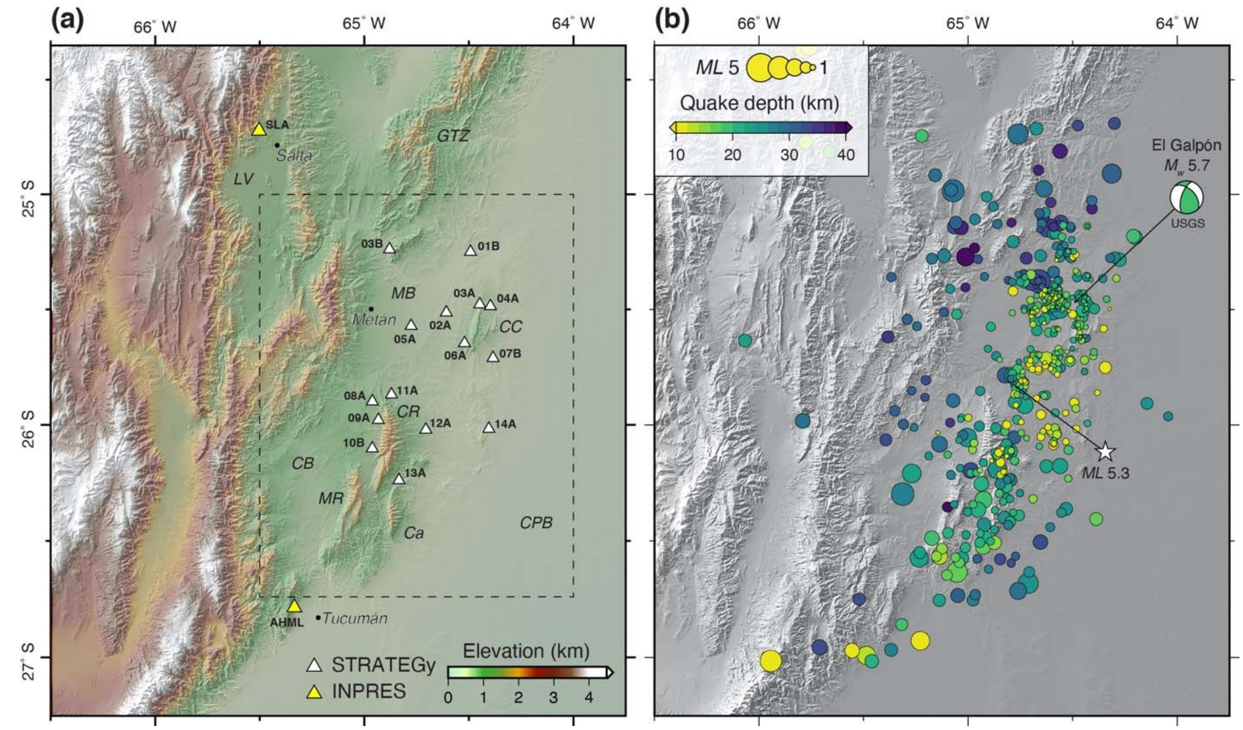

Figure 2 Local setting and relocated shallow seismicity. (a) Distribution of seismic stations used in the analysis including temporary STRATEGy installations (white triangles) and permanent stations of the Argentinian national seismological service INPRES (yellow triangles). Dashed box outlines the region shown in Figure 4a. (b) Detected and relocated local, crustal seismicity (depths ≤ 40 km) recorded during the installation period of the STRATEGy network. Circles are color-coded by depth and size is scaled to *ML*. Also shown are the USGS focal mechanism for the 2015 El Galpón earthquake and the ISC location of the preceding 2015 *ML* 5.3 Rosario de la Frontera event. GTZ=Garrapatas transverse zone; LV=Lerma Valley; MB=Metán Basin; CC=Cerro Colorado; CR=La Candelaria Range; CB=Choromoro Basin, MR=Medina Range; Ca=Campos Range, CPB=Chaco-Paraná Basin.

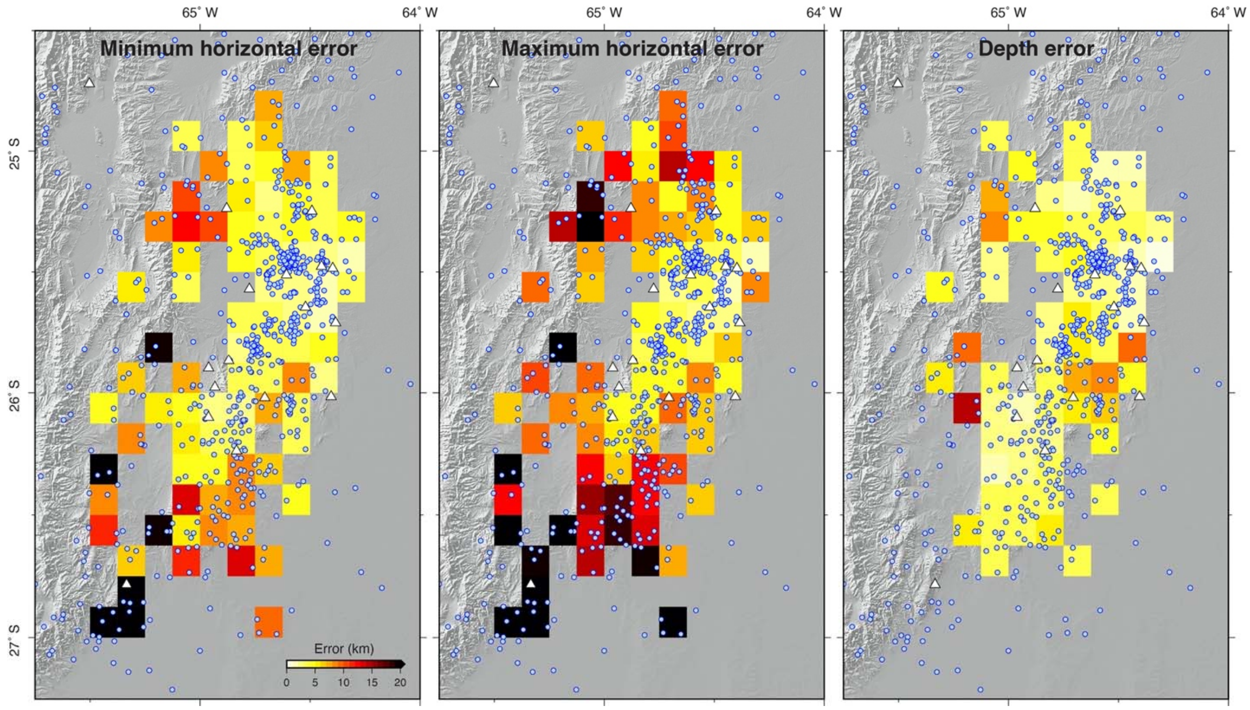

Figure 3 Quality of the STRATEGy earthquake dataset locations with event uncertainties averaged in a 0.125° x 0.125° grid; only nodes with at least two events are shown. STRATEGy and INPRES station locations are shown as white triangles and the epicenter locations for all events recorded during the network deployment are small blue circles. Errors are given as the 95% confidence interval for the location estimate. Minimum and maximum horizontal errors are defined as the semi-minor and semi-major axes of the error ellipses for the epicenter solution. Depth errors are derived independently from horizontal errors during the last location inversion step of the location, which might result in fixed event depths and a smaller number of grid nodes compared to the horizontal errors.

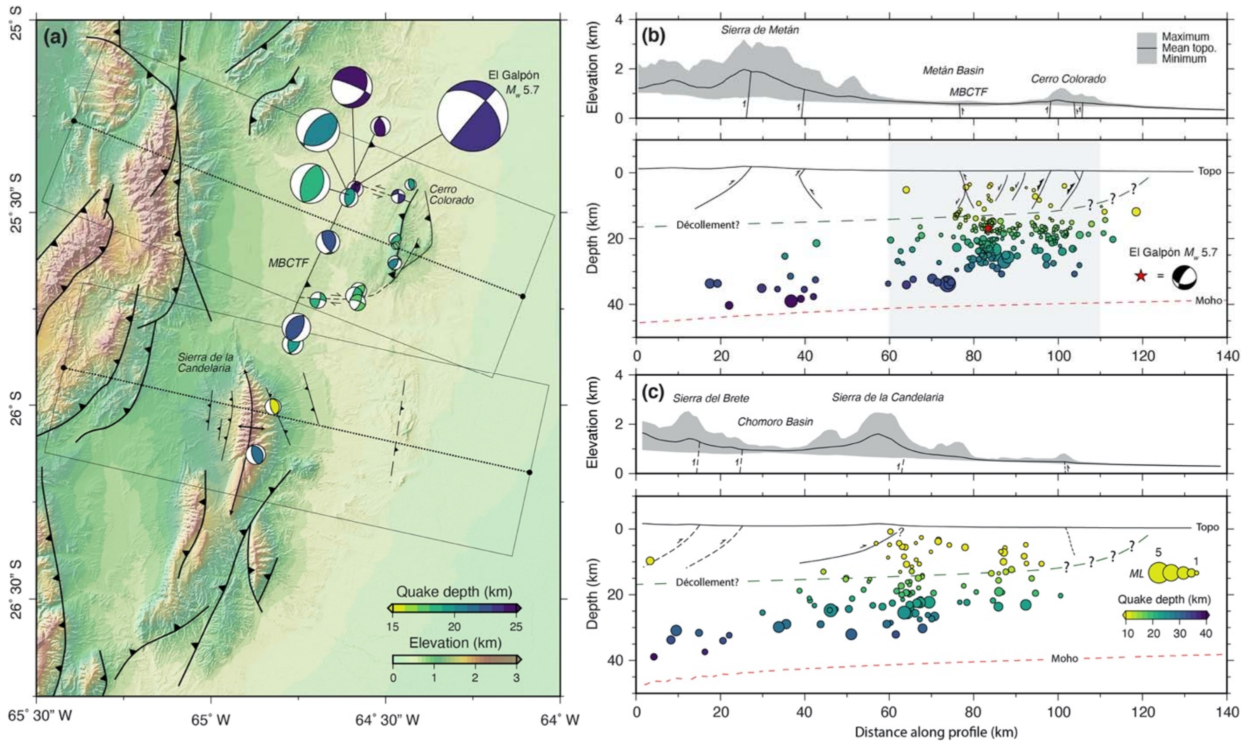

Figure 4 SBS seismotectonic map and cross-sections. (a) Topography and structures with Quaternary activity, modified after *Arnous et al.* [2020]; *Iaffa et al.* [2013]; *Iaffa et al.* [2011]; *Kley et al.* [1999]; and *Kley et al.* [2005]. Focal mechanisms derived from the first-motion polarity analysis are scaled with size to *ML* and color-coded by depth. The 2015 El Galpón event moment tensor solution from the USGS is based on teleseismic observations. The locations of the swath profiles shown in (a) are indicated with dashed lines and associated rectangles. (b) Northern profile across the Metán Basin and Cerro Colorado with vertically exaggerated swath topography and projected earthquake locations. MBCTF: Metán Basin Central Thrust Fault.; (c) Southern profile across the Choromoro Basin and Sierra de La Candelaria. Shallow subsurface fault geometries in (a) and (b) are primarily based on seismic reflection results presented in *Iaffa et al.* [2011], *Iaffa et al.* [2013], and *Arnous et al.* [2020], with fault depths typically limited to depths less than 15 km. The location of an inferred rift-related décollement is from *Grier et al.* [1991]. The Moho location in (b) and (c) is from *Tassara and Echaurren* [2012].

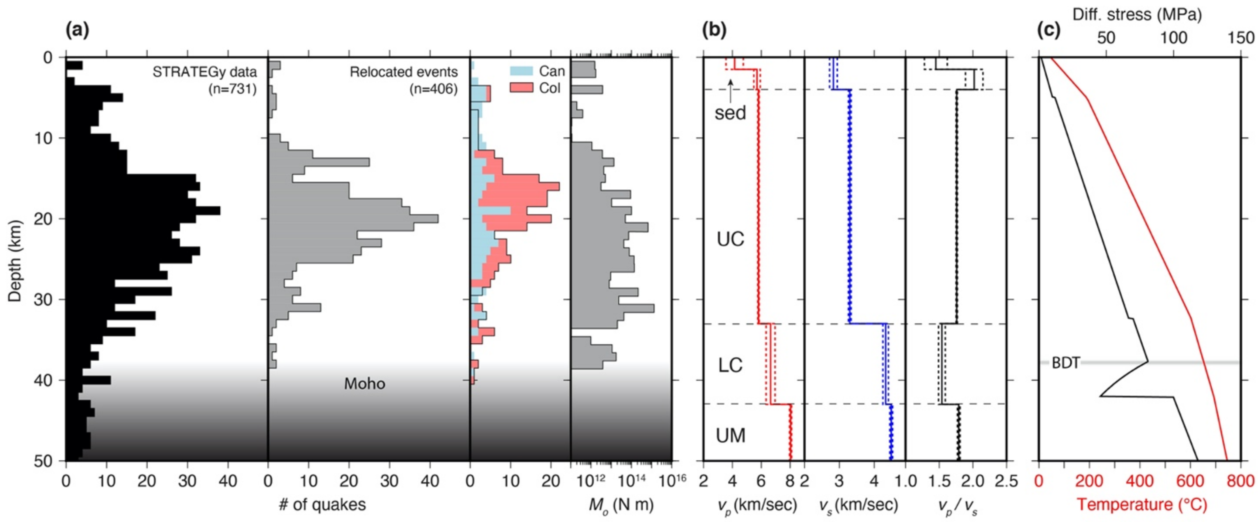

Figure 5 (a) SBS primary earthquake hypocenter depth distribution in 1 km bins from the STRATEGy deployment, relocated events (gray), relocated events for the northern SBS in the vicinity of Cerro Colorado (red) and the southern SBS in the area of the La Candelaria Range (blue), and cumulative seismic moment release with depth for the relocated catalogue based on the conversion law of *Parolai et al.* [2007]. See Figure 4 for the profile locations and Figures 1 and 2 for map views of the seismicity. (b) Seismic velocity model inverted in section XX for V_P (red), V_S (blue) and V_P/V_S ratio (black) with dashed uncertainty envelopes. sed=sediments; UC=upper crust; LC=lower crust, UM=upper mantle. (c) Yield-strength envelope (YSE; black) and temperature (red) for the southern SBS. Gray horizontal line is the location of the theoretical brittle-ductile transition (BDT) zone that coincides with the observed decrease in seismicity. Inflections in the differential stress curve indicate changes in the model rheology from a UC composed of quartzo-diorite, a LC comprised of mafic granulite, and a coefficient of friction of 0.1. See *Ibarra et al.* [2021] for more information on YSE construction.

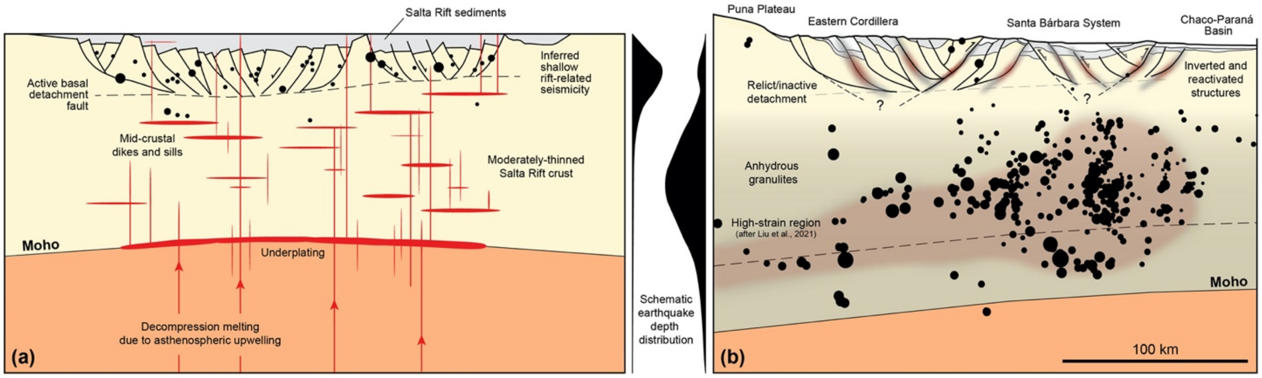

Figure 6 Conceptual model of Santa Bárbara System (SBS) deformation, rheology, and seismicity (not to scale). (a) Setting during the late Cretaceous phase of continental extension. The upper crustal cross-section with numerous Salta Rift-related normal faults that root in a shallow detachment zone are from *Grier et al.* [1991]. During the late Cretaceous, crustal thinning was accompanied by surface faulting, decompression melting, associated magmatism, and the formation of dike and sill complexes that likely caused and/or contributed to large-scale dehydration and the creation of anhydrous granulites in the middle and lower crust beneath the active rift. This view of the early rift stage of continental extension including the magmatic plumbing system and the distribution of shallow seismicity is schematic and conceptually based on studies across active rifts zones [e.g., the East African Rift System; *Albaric et al.*, 2009; *Biggs et al.*, 2021; *Corti*, 2012; *Craig and Jackson*, 2021; *Ebinger*, 2005; *Reiss et al.*, 2021]. (b) Present-day view of compressional deformation associated with Andean orogenesis. Shallow structures including inverted and reactivated faults are from *Grier et al.* [1991]. Earthquakes are from this study. The tadpole-shaped, high-strain region that generally coincides with the observed seismicity is based on the geodynamic modeling results of *Liu et al.* [2022] and is also guided by our new seismic velocity profiles and yield-strength envelope (Figure 5). The *Liu et al.* [2022] model also shows localized strain accumulation in the vicinity of the shallow structures that is separate from the deeper deformation zone. It remains unclear if and how the shallow, active faults connect to the deeper seismicity.

References

Abascal, L. d. V. (2005), Combined thin-skinned and thick-skinned deformation in the central Andean foreland of northwestern Argentina, *Journal of South American Earth Sciences*, *19*(1), 75-81, doi:https://doi.org/10.1016/j.jsames.2005.01.004.

Akyol, N., L. Zhu, B. J. Mitchell, H. Sözbilir, and K. Kekovalı (2006), Crustal structure and local seismicity in western Anatolia, *Geophysical Journal International*, *166*(3), 1259-1269, doi:10.1111/j.1365-246X.2006.03053.x.

Albaric, J., J. Déverchère, C. Petit, J. Perrot, and B. Le Gall (2009), Crustal rheology and depth distribution of earthquakes: Insights from the central and southern East African Rift System, *Tectonophysics*, *468*(1), 28-41, doi:https://doi.org/10.1016/j.tecto.2008.05.021.

Allmendinger, R. W., and T. Gubbels (1996), Pure and simple shear plateau uplift, Altiplano-Puna, Argentina and Bolivia, *Tectonophysics*, *259*(1), 1-13, doi:https://doi.org/10.1016/0040-1951(96)00024-8.

Alvarado, P., and V. Ramos (2011), Earthquake deformation in the northwestern Sierras Pampeanas of Argentina based on seismic waveform modeling, *Journal of Geodynamics*, *51*, 205-218, doi:10.1016/j.jog.2010.08.002.

Amitrano, D. (2003), Brittle-ductile transition and associated seismicity: Experimental and numerical studies and relationship with the b value, *Journal of Geophysical Research: Solid Earth*, *108*(B1), doi:https://doi.org/10.1029/2001JB000680.

Ammirati, J.-B., C. Mackaman-Lofland, M. Zeckra, and K. Gobron (2022), Stress transmission along mid-crustal faults highlighted by the 2021 Mw 6.5 San Juan (Argentina) earthquake, *Sci Rep-Uk*, *12*(1), 17939, doi:10.1038/s41598-022-22752-6.

Arnous, A., M. Zeckra, A. Venerdini, P. Alvarado, R. Arrowsmith, J. Guillemoteau, A. Landgraf, A. Gutiérrez, and M. R. Strecker (2020), Neotectonic Activity in the Low-Strain Broken Foreland (Santa Bárbara System) of the North-Western Argentinean Andes (26°S), *Lithosphere*, *2020*(1), 1-25, doi:10.2113/2020/8888588.

Asch, G., et al. (2006), Seismological Studies of the Central and Southern Andes, in *The Andes: Active Subduction Orogeny*, edited by O. Oncken, G. Chong, G. Franz, P. Giese, H.-J. Götze, V. A. Ramos, M. R. Strecker and P. Wigger, pp. 443-457, Springer Berlin Heidelberg, Berlin, Heidelberg, doi:10.1007/978-3-540-48684-8_21.

Babeyko, A. Y., and S. V. Sobolev (2005), Quantifying different modes of the late Cenozoic shortening in the Central Andes, *Geology*, *33*(8), 621-624.

Barcelona, H., G. Peri, J. Tobal, L. Sagripanti, and A. Favetto (2014), Tectonic activity revealed by morphostructural analysis: Development of the Sierra de la Candelaria range, northwestern Argentina, *Journal of South American Earth Sciences*, *56*, 376-395, doi:https://doi.org/10.1016/j.jsames.2014.10.002.

Behn, M. D., W. R. Buck, and I. S. Sacks (2006), Topographic controls on dike injection in volcanic rift zones, *Earth Planet. Sci. Lett.*, *246*, 188-196.

Bellahsen, N., M. Sebrier, and L. Siame (2016), Crustal shortening at the Sierra Pie de Palo (Sierras Pampeanas, Argentina): near-surface basement folding and thrusting, *Geological Magazine*, *153*(5-6), 992-1012, doi:10.1017/S0016756816000467.

Beyreuther, M., R. Barsch, L. Krischer, T. Megies, Y. Behr, and J. Wassermann (2010), ObsPy: A Python Toolbox for Seismology, *Seismological Research Letters*, *81*(3), 530-533, doi:10.1785/gssrl.81.3.530.

Biggs, J., A. Ayele, T. P. Fischer, K. Fontijn, W. Hutchison, E. Kazimoto, K. Whaler, and T. J. Wright (2021), Volcanic activity and hazard in the East African Rift Zone, *Nature Communications*, *12*(1), 6881, doi:10.1038/s41467-021-27166-y.

Bookhagen, B., and M. Strecker (2008), Orographic barriers, high-resolution TRMM rainfall, and relief variations along the eastern Andes, *Geophysical Research Letters*, *35*(L06403,), doi:10.1029/2007GL032011.

Bormann, P., and J. W. Dewey (2012), The new IASPEI standards for determining magnitudes from digital data and their relation to classical magnitudes, *New Manual of Seismological Observatory Practice 2 (NMSOP-2)*, 1-44, doi:10.2312/GFZ.NMSOP-2_IS_3.3.

Brooks, B. A., M. Bevis, R. J. Smalley, E. Kendrick, R. Manceda, E. Lauria, R. Maturana, and M. Araujo (2003), Crustal Motion in the Southern Andes (26°-36°S): Do the Andes Behave Like a Microplate?, *Geochemistry, Geophysics, Geosystems*, *4*(10), doi:10.1029/2003GC000505.

Brooks, B. A., et al. (2011), Orogenic-wedge deformation and potential for great earthquakes in the central Andean backarc, *Nature Geoscience*, *4*(6), 380-383, doi:Doi 10.1038/Ngeo1143.

Buck, W. R., L. L. Lavier, and A. N. B. Poliakov (2005), Modes of faulting at mid-ocean ridges, *Nature*, *434*(7034), 719-723, doi:10.1038/nature03358.

Burbank, McLean, Bullen, Abdrakhmatov, and Miller (1999), Partitioning of intermontane basins by thrust-related folding, Tien Shan, Kyrgyzstan, *Basin Research*, *11*(1), 75-92, doi:https://doi.org/10.1046/j.1365-2117.1999.00086.x.

Cahill, T., and B. L. Isacks (1992), Seismicity and shape of the subducted Nazca Plate, *Journal of Geophysical Research: Solid Earth*, *97*(B12), 17503-17529, doi:https://doi.org/10.1029/92JB00493.

Cahill, T., B. L. Isacks, D. Whitman, J.-L. Chatelain, A. Perez, and J. M. Chiu (1992), Seismicity and tectonics in Jujuy Province, northwestern Argentina, *Tectonics*, *11*(5), 944-959, doi:10.1029/92tc00215.

Carrera, N., and J. A. Muñoz (2008), Thrusting evolution in the southern Cordillera Oriental (northern Argentine Andes): Constraints from growth strata, *Tectonophysics*, *459*(1), 107-122, doi:https://doi.org/10.1016/j.tecto.2007.11.068.

Casa, A., M. Yamin, Wright, C. Costa, M. Coppolecchia, M. Cegarra, and F. Hongn (2014), Deformaciones Cuaternarias de la República Argentina, Sistema de Información Geográfica, *Instituto de Geología y Recursos Minerales. Servicio Geológico Minero Argentino*, *v2.0*.

Cesca, S., and F. Grigoli (2015), Chapter Two - Full Waveform Seismological Advances for Microseismic Monitoring, in *Advances in Geophysics*, edited by R. Dmowska, pp. 169-228, Elsevier, doi:https://doi.org/10.1016/bs.agph.2014.12.002.

Christensen, N. I. (1996), Poisson's ratio and crustal seismology, *Journal of Geophysical Research: Solid Earth*, *101*(B2), 3139-3156, doi:https://doi.org/10.1029/95JB03446.

Christensen, N. I., and W. D. Mooney (1995), Seismic velocity structure and composition of the continental crust: A global view, *Journal of Geophysical Research: Solid Earth*, *100*(B6), 9761-9788, doi:https://doi.org/10.1029/95JB00259.

Comino, J. Á. L., S. Heimann, S. Cesca, C. Milkereit, T. Dahm, and A. Zang (2017), Automated Full Waveform Detection and Location Algorithm of Acoustic Emissions from Hydraulic Fracturing Experiment, *Procedia Engineering*, *191*, 697-702, doi:https://doi.org/10.1016/j.proeng.2017.05.234.

Copley, A., J.-P. Avouac, J. Hollingsworth, and S. Leprince (2011), The 2001 Mw 7.6 Bhuj earthquake, low fault friction, and the crustal support of plate driving forces in India, *Journal of Geophysical Research: Solid Earth*, *116*(B8), doi:https://doi.org/10.1029/2010JB008137.

Corti, G. (2012), Evolution and characteristics of continental rifting: Analog modeling-inspired view and comparison with examples from the East African Rift System, *Tectonophysics*, *522-523*, 1-33, doi:https://doi.org/10.1016/j.tecto.2011.06.010.

Costa, C., et al. (2020), Hazardous faults of South America; compilation and overview, *Journal of South American Earth Sciences*, *104*, 102837, doi:https://doi.org/10.1016/j.jsames.2020.102837.

Craig, T. J., A. Copley, and J. Jackson (2012), Thermal and tectonic consequences of India underthrusting Tibet, *Earth and Planetary Science Letters*, *353-354*, 231-239, doi:https://doi.org/10.1016/j.epsl.2012.07.010.

Craig, T. J., and J. A. Jackson (2021), Variations in the Seismogenic Thickness of East Africa, *Journal of Geophysical Research: Solid Earth*, *126*(3), e2020JB020754, doi:https://doi.org/10.1029/2020JB020754.

Cristallini, E., A. Cominguez, V. Ramos, and E. Mercerat (2004), Basement double-wedge thrusting in the Northern Sierras Pampeanas of Argentina (27°S) - Constraints from deep seismic reflection, edited, pp. 65-90.

Cristallini, E., A. H. Cominguez, and V. A. Ramos (1997), Deep structure of the Metan-Guachipas region: tectonic inversion in Northwestern Argentina, *Journal of South American Earth Sciences*, *10*(5), 403-421, doi:https://doi.org/10.1016/S0895-9811(97)00026-6.

Currie, C. A., and R. D. Hyndman (2006), The thermal structure of subduction zone back arcs, *J Geophys Res-Sol Ea*, *111*(B8), doi:10.1029/2005jb004024.

Dahlen, F. A. (1990), Critical taper model of fold-and-thrust belts and accretionary wedges, *Annual Review of Earth and Planetary Sciences*, *18*, 55-99.

Dahlen, F. A., J. Suppe, and D. Davis (1984), Mechanics of fold-and-thrust belts and accretionary wedges-cohesive Coulomb theory, *Journal of Geophysical Research*, *89*(NB12), 87-101, doi:10.1029/JB089iB12p10087.

Davis, D., J. Suppe, and F. A. Dahlen (1983), Mechanics of fold-and-thrust belts and accretionary wedges, *Journal of Geophysical Research*, *88*(NB2), 1153-1172, doi:10.1029/JB088iB02p01153.

Devlin, S., B. L. Isacks, M. E. Pritchard, W. D. Barnhart, and R. B. Lohman (2012), Depths and focal mechanisms of crustal earthquakes in the central Andes determined from teleseismic waveform analysis and InSAR, *Tectonics*, *31*(2), doi:https://doi.org/10.1029/2011TC002914.

Drew, J., R. S. White, F. Tilmann, and J. Tarasewicz (2013), Coalescence microseismic mapping, *Geophysical Journal International*, *195*(3), 1773-1785, doi:10.1093/gji/ggt331.

Ebinger, C. (2005), Continental break-up: The East African perspective, *Astronomy & Geophysics*, *46*(2), 2.16-12.21, doi:10.1111/j.1468-4004.2005.46216.x.

Figueroa, S., J. R. Weiss, F. Hongn, H. Pingel, L. Escalante, L. Elías, R. G. Aranda-Viana, and M. R. Strecker (2021), Late Pleistocene to Recent Deformation in the Thick-Skinned Fold-and-Thrust Belt of Northwestern Argentina (Central Calchaquí Valley, 26°S), *Tectonics*, *40*(1), e2020TC006394, doi:https://doi.org/10.1029/2020TC006394.

Franz, G., F. Lucassen, W. Kramer, R. Trumbull, R. Romer, H.-G. Wilke, J. Viramonte, R. Becchio, and W. Siebel (2006), Crustal Evolution at the Central Andean Continental Margin: a Geochemical Record of Crustal Growth, Recycling and Destruction, edited, pp. 45-64, doi:10.1007/978-3-540-48684-8_3.

Galliski, M. A., and J. G. Viramonte (1988), The Cretaceous paleorift in northwestern Argentina: A petrologic approach, *Journal of South American Earth Sciences*, *1*(4), 329-342, doi:https://doi.org/10.1016/0895-9811(88)90021-1.

García, V. H., F. Hongn, and E. O. Cristallini (2013), Late Miocene to recent morphotectonic evolution and potential seismic hazard of the northern Lerma valley: Clues from Lomas de Medeiros, Cordillera Oriental, NW Argentina, *Tectonophysics*, *608*, 1238-1253, doi:https://doi.org/10.1016/j.tecto.2013.06.021.

García, V. H., F. Hongn, D. Yagupsky, H. Pingel, T. Kinnaird, D. Winocur, E. Cristallini, R. A. J. Robinson, and M. R. Strecker (2019), Late Quaternary tectonics controlled by fault reactivation. Insights from a local transpressional system in the intermontane Lerma valley, Cordillera Oriental, NW Argentina, *Journal of Structural Geology*, *128*, 103875, doi:https://doi.org/10.1016/j.jsg.2019.103875.

Gioncada, A., L. Vezzoli, M. R, R. Omarini, P. Nonnotte, and H. Guillou (2010), Pliocene intraplate-type volcanism in the Andean foreland at 26°10′S, 64°40′W (NW Argentina): Implications for magmatic and structural evolution of the Central Andes, *Lithosphere*, *2*, 153-171, doi:10.1130/L81.1.

Grier, M. E., J. A. Salfity, and R. W. Allmendinger (1991), Andean reactivation of the Cretaceous Salta rift, northwestern Argentina, *Journal of South American Earth Sciences*, *4*(4), 351-372, doi:https://doi.org/10.1016/0895-9811(91)90007-8.

Grigoli, F., S. Cesca, M. Vassallo, and T. Dahm (2013), Automated Seismic Event Location by Travel-Time Stacking: An Application to Mining Induced Seismicity, *Seismological Research Letters*, *84*(4), 666-677, doi:10.1785/0220120191.

Gubbels, T. L., B. L. Isacks, and E. Farrar (1993), High-level surfaces, plateau uplift, and foreland development, Bolivian Central Andes, *Geology*, *21*(8), 695-698.

Hain, M. P., M. R. Strecker, B. Bookhagen, R. N. Alonso, H. Pingel, and A. K. Schmitt (2011), Neogene to Quaternary broken foreland formation and sedimentation dynamics in the Andes of NW Argentina (25°S), *Tectonics*, *30*(2), doi:10.1029/2010tc002703.

Heimann, S., H. Vasyura-Bathke, H. Sudhaus, M. P. Isken, M. Kriegerowski, A. Steinberg, and T. Dahm (2019), A Python framework for efficient use of pre-computed Green's functions in seismological and other physical forward and inverse source problems, *Solid Earth*, *10*(6), 1921-1935, doi:10.5194/se-10-1921-2019.

Hibert, C., et al. (2014), Automated identification, location, and volume estimation of rockfalls at Piton de la Fournaise volcano, *Journal of Geophysical Research: Earth Surface*, *119*(5), 1082-1105, doi:https://doi.org/10.1002/2013JF002970.

Hilley, G. E., P. M. Blisniuk, and M. R. Strecker (2005), Mechanics and erosion of basement-cored uplift provinces, *Journal of Geophysical Research: Solid Earth*, *110*(B12), doi:10.1029/2005jb003704.

Hilley, G. E., and M. R. Strecker (2004), Steady state erosion of critical Coulomb wedges with applications to Taiwan and the Himalaya, *J Geophys Res-Sol Ea*, *109*(B1), doi:10.1029/2002jb002284.

Husen, S., E. Kissling, N. Deichmann, S. Wiemer, D. Giardini, and M. Baer (2003), Probabilistic earthquake location in complex three-dimensional velocity models: Application to Switzerland, *Journal of Geophysical Research: Solid Earth*, *108*(B2), doi:https://doi.org/10.1029/2002JB001778.

Iaffa, D., F. Sàbat, J. Muñoz, and N. Carrera (2013), Basin fragmentation controlled by tectonic inversion and basement uplift in Sierras Pampeanas and Santa Bárbara System, northwest Argentina, *Geological Society London Special Publications*, *377*, doi:10.1144/SP377.13.

Iaffa, D. N., F. Sàbat, J. A. Muñoz, R. Mon, and A. A. Gutierrez (2011), The role of inherited structures in a foreland basin evolution. The Metán Basin in NW Argentina, *Journal of Structural Geology*, *33*(12), 1816-1828, doi:https://doi.org/10.1016/j.jsg.2011.09.005.

Ibarra, F., S. Liu, C. Meeßen, C. B. Prezzi, J. Bott, M. Scheck-Wenderoth, S. Sobolev, and M. R. Strecker (2019), 3D data-derived lithospheric structure of the Central Andes and its implications for deformation: Insights from gravity and geodynamic modelling, *Tectonophysics*, *766*, 453-468, doi:https://doi.org/10.1016/j.tecto.2019.06.025.

Ibarra, F., C. B. Prezzi, J. Bott, M. Scheck-Wenderoth, and M. R. Strecker (2021), Distribution of Temperature and Strength in the Central Andean Lithosphere and Its Relationship to Seismicity and Active Deformation, *Journal of Geophysical Research: Solid Earth*, *126*(5), e2020JB021231, doi:https://doi.org/10.1029/2020JB021231.

Jackson, J., K. Priestley, and B. Emmerson (2008), New views on the structure and rheology of the lithosphere, *Journal of the Geological Society*, *165*(2), 453-465, doi:10.1144/0016-76492007-109.

Jackson, J. A., H. Austrheim, D. McKenzie, and K. Priestley (2004), Metastability, mechanical strength, and the support of mountain belts, *Geology*, *32*(7), 625-628, doi:10.1130/g20397.1.

Jordan, T. E., and R. W. Allmendinger (1986), The Sierras Pampeanas of Argentina; a modern analogue of Rocky Mountain foreland deformation, *American Journal of Science*, *286*, 737-764, doi:10.2475/ajs.286.10.737.

Jordan, T. E., B. L. Isacks, R. W. Allmendinger, J. A. Brewer, V. A. Ramos, and C. J. Ando (1983), Andean tectonics related to geometry of subducted Nazca plate, *GSA Bulletin*, *94*(3), 341-361, doi:10.1130/0016-7606(1983)94<341:Atrtgo>2.0.Co;2.

Kennett, B. L. N., E. R. Engdahl, and R. Buland (1995), Constraints on seismic velocities in the Earth from traveltimes, *Geophysical Journal International*, *122*(1), 108-124, doi:10.1111/j.1365-246X.1995.tb03540.x.

Kirby, S., R. E. Engdahl, and R. Denlinger (1996), Intermediate-Depth Intraslab Earthquakes and Arc Volcanism as Physical Expressions of Crustal and Uppermost Mantle Metamorphism in Subducting Slabs, in *Subduction*, edited, pp. 195-214, doi:https://doi.org/10.1029/GM096p0195.

Kissling, E., W. L. Ellsworth, D. Eberhart-Phillips, and U. Kradolfer (1994), Initial reference models in local earthquake tomography, *Journal of Geophysical Research: Solid Earth*, *99*(B10), 19635-19646, doi:https://doi.org/10.1029/93JB03138.

Kley, J., and C. R. Monaldi (2002), Tectonic inversion in the Santa Barbara System of the central Andean foreland thrust belt, northwestern Argentina, *Tectonics*, *21*(6), 11-11-11-18, doi:10.1029/2002tc902003.

Kley, J., C. R. Monaldi, and J. Salfity (1996), *Along-strike segmentation of the Andean foreland*.

Kley, J., C. R. Monaldi, and J. A. Salfity (1999), Along-strike segmentation of the Andean foreland; causes and consequences, *Tectonophysics*, *301*(1-2), 75-94.

Kley, J., E. A. Rossello, C. R. Monaldi, and B. Habighorst (2005), Seismic and field evidence for selective inversion of Cretaceous normal faults, Salta rift, northwest Argentina, *Tectonophysics*, *399*(1), 155-172, doi:https://doi.org/10.1016/j.tecto.2004.12.020.

Lacombe, O., and N. Bellahsen (2016), Thick-skinned tectonics and basement-involved fold–thrust belts: insights from selected Cenozoic orogens, *Geological Magazine*, *153*(5-6), 763-810, doi:10.1017/S0016756816000078.

Lamb, S. (2000), Active deformation in the Bolivian Andes, South America, *Journal of Geophysical Research*, *105*(B11), 25,627-625,653.

Langet, N., A. Maggi, A. Michelini, and F. Brenguier (2014), Continuous Kurtosis-Based Migration for Seismic Event Detection and Location, with Application to Piton de la Fournaise Volcano, La Réunion, *Bulletin of the Seismological Society of America*, *104*(1), 229-246, doi:10.1785/0120130107.

Laske, G., G. Masters, Z. Ma, and M. Pasyanos (2013), Update on CRUST1.0 - A 1-degree global model of Earth's crust, *Abstract EGU2013-2658 presented at 2013 Geophys. Res. Abstracts 15*, *15*, 2658.

Liu, S., S. V. Sobolev, A. Y. Babeyko, and M. V. Pons-Rallo (2022), Controls of the Foreland Deformation Pattern in the Orogen-Foreland Shortening System: Constraints from High-Resolution Geodynamic Models, *Earth and Space Science Open Archive*, 35, doi:doi:10.1002/essoar.10508507.2.

Lucassen, F., G. Franz, R. Romer, F. Schultz, P. Dulski, and K. Wemmer (2007), Pre-Cenozoic intra-plate magmatism along the Central Andes (17–34°S): Composition of the mantle at an active margin, *Lithos*, *99*, 312-338, doi:10.1016/j.lithos.2007.06.007.

Lucassen, F., G. Franz, J. Viramonte, R. L. Romer, P. Dulski, and A. Lang (2005), The late Cretaceous lithospheric mantle beneath the Central Andes: Evidence from phase equilibria and composition of mantle xenoliths, *Lithos*, *82*, 379-406, doi:10.1016/j.lithos.2004.08.002.

Lucassen, F., S. Lewerenz, G. Franz, J. Viramonte, and K. Mezger (1999), Metamorphism, isotopic ages and composition of lower crustal granulite xenoliths from the Cretaceous Salta Rift, Argentina, *Contributions to Mineralogy and Petrology*, *134*, 325, doi:10.1007/s004100050488.

Maggi, A., J. A. Jackson, D. McKenzie, and K. Priestley (2000), Earthquake focal depths, effective elastic thickness, and the strength of the continental lithosphere, *Geology*, *28*(6), 495-498, doi:10.1130/0091-7613(2000)28<495:Efdeet>2.0.Co;2.

Marquillas, R. A., C. del Papa, and I. F. Sabino (2005), Sedimentary aspects and paleoenvironmental evolution of a rift basin: Salta Group (Cretaceous–Paleogene), northwestern Argentina, *Int J Earth Sci*, *94*(1), 94-113, doi:10.1007/s00531-004-0443-2.

Marshak, S., K. Karlstrom, and J. M. Timmons (2000), Inversion of Proterozoic extensional faults: An explanation for the pattern of Laramide and Ancestral Rockies intracratonic deformation, United States, *Geology*, *28*(8), 735-738, doi:10.1130/0091-7613(2000)28<735:Iopefa>2.0.Co;2.

McFarland, P. K., R. A. Bennett, P. Alvarado, and P. G. DeCelles (2017), Rapid Geodetic Shortening Across the Eastern Cordillera of NW Argentina Observed by the Puna-Andes GPS Array, *Journal of Geophysical Research: Solid Earth*, *122*(10), 8600-8623, doi:10.1002/2017jb014739.

Michailos, K., E. G. C. Smith, C. J. Chamberlain, M. K. Savage, and J. Townend (2019), Variations in Seismogenic Thickness Along the Central Alpine Fault, New Zealand, Revealed by a Decade's Relocated Microseismicity, *Geochemistry, Geophysics, Geosystems*, *20*(1), 470-486, doi:https://doi.org/10.1029/2018GC007743.

Mon, R. (1976), The structure of the eastern border of the Andes in north-western Argentina, *Geologische Rundschau*, *65*(1), 211-222, doi:10.1007/BF01808464.

Mon, R., and A. A. Gutiérrez (2007), Estructura del extremo sur del sistema subandino (provincias de Salta, Santiago del Estero y Tucumán), *Revista de la Asociación Geológica Argentina*, *62*(1), 62-68.

Mon, R., and J. A. Salfity (1995), Tectonic Evolution of the Andes of Northern Argentina, in *Petroleum Basins of South America*, edited by A. J. Tankard, R. S. Soruco and H. J. Welsink, pp. 269-283, American Association of Petroleum Geologists, doi:10.1306/m62593c12.

Monsalve, G., J. S. Jaramillo, A. Cardona, V. Schulte-Pelkum, G. Posada, V. Valencia, and E. Poveda (2019), Deep Crustal Faults, Shear Zones, and Magmatism in the Eastern Cordillera of Colombia: Growth of a Plateau From Teleseismic Receiver Function and Geochemical Mio-

Pliocene Volcanism Constraints, *Journal of Geophysical Research: Solid Earth*, *124*(9), 9833-9851, doi:https://doi.org/10.1029/2019JB017835.

Monsalve, G., A. Sheehan, V. Schulte-Pelkum, S. Rajaure, M. R. Pandey, and F. Wu (2006), Seismicity and one-dimensional velocity structure of the Himalayan collision zone: Earthquakes in the crust and upper mantle, *Journal of Geophysical Research: Solid Earth*, *111*(B10), doi:https://doi.org/10.1029/2005JB004062.

Mori, J., and R. E. Abercrombie (1997), Depth dependence of earthquake frequency-magnitude distributions in California: Implications for rupture initiation, *Journal of Geophysical Research: Solid Earth*, *102*(B7), 15081-15090, doi:https://doi.org/10.1029/97JB01356.

Mulcahy, P., C. Chen, S. M. Kay, L. D. Brown, B. L. Isacks, E. Sandvol, B. Heit, X. Yuan, and B. L. Coira (2014), Central Andean mantle and crustal seismicity beneath the Southern Puna plateau and the northern margin of the Chilean-Pampean flat slab, *Tectonics*, *33*(8), 1636-1658, doi:https://doi.org/10.1002/2013TC003393.

Ortiz, G., A. L. Stevens Goddard, J. C. Fosdick, P. Alvarado, B. Carrapa, and E. Cristofolini (2021), Fault reactivation in the Sierras Pampeanas resolved across Andean extensional and compressional regimes using thermochronologic modeling, *Journal of South American Earth Sciences*, *112*, 103533, doi:https://doi.org/10.1016/j.jsames.2021.103533.

Parolai, S., D. Bindi, E. Durukal, H. Grosser, and C. Milkereit (2007), Source Parameters and Seismic Moment–Magnitude Scaling for Northwestern Turkey, *Bulletin of the Seismological Society of America*, *97*(2), 655-660, doi:10.1785/0120060180.

Pearson, D. M., P. Kapp, P. G. DeCelles, P. W. Reiners, G. E. Gehrels, M. N. Ducea, and A. Pullen (2013), Influence of pre-Andean crustal structure on Cenozoic thrust belt kinematics and shortening magnitude: Northwestern Argentina, *Geosphere*, *9*(6), 1766-1782, doi:10.1130/ges00923.1.

Perucca, L., and S. Moreiras (2009), Seismic and Volcanic Hazards in Argentina, *Developments in Earth Surface Processes*, *13*, doi:10.1016/S0928-2025(08)10014-1.

Pingel, H., M. R. Strecker, R. N. Alonso, and A. K. Schmitt (2013), Neotectonic basin and landscape evolution in the Eastern Cordillera of NW Argentina, Humahuaca Basin (~24°S), *Basin Research*, *25*(5), 554-573, doi:https://doi.org/10.1111/bre.12016.

Pugh, D., and R. White (2018), MTfit: A Bayesian Approach to Seismic Moment Tensor Inversion, *Seismological Research Letters*, *89*, doi:10.1785/0220170273.

Pugh, D. J., R. S. White, and P. A. F. Christie (2016), A Bayesian method for microseismic source inversion, *Geophysical Journal International*, *206*(2), 1009-1038, doi:10.1093/gji/ggw186.

Ramezani Ziarani, M., B. Bookhagen, T. Schmidt, J. Wickert, A. de la Torre, and R. Hierro (2019), Using Convective Available Potential Energy (CAPE) and Dew-Point Temperature to Characterize Rainfall-Extreme Events in the South-Central Andes, *Atmosphere*, *10*(7), 379.

Ramos, V. (1988), The tectonics of the Central Andes; 30 to 33 S latitude, *Special Paper of the Geological Society of America*, *218*, 31-54, doi:10.1130/SPE218-p31.

Ramos, V. (2000), Las provincias geológicas del territorio argentino, *Geología Argentina*, *29*, 41-96.

Ramos, V. A., R. Alonso, and M. Strecker (2006), Estructura y neotectónica de Las Lomas de Olmedo, zona de transición entre los Sistemas Subandino y de Santa Bárbara, provincia de Salta, *Revista de la Asociacion Geologica Argentina*, *61*, 579-588.

Ramos, V. A., E. O. Cristallini, and D. J. Pérez (2002), The Pampean flat-slab of the Central Andes, *Journal of South American Earth Sciences*, *15*(1), 59-78, doi:https://doi.org/10.1016/S0895-9811(02)00006-8.

Ramos, V. A., T. Zapata, E. Cristallini, and A. Introcaso (2004), The Andean thrust system-Latitudinal variations in structural styles and orogenic shortening, in *Thrust tectonics and hydrocarbon systems: AAPG Memoir 82*, edited by K. R. McClay, pp. 30-50.

Rapela, C. W., R. J. Pankhurst, C. Casquet, E. Baldo, C. Galindo, C. M. Fanning, and J. M. Dahlquist (2010), The Western Sierras Pampeanas: Protracted Grenville-age history (1330–1030Ma) of intra-oceanic arcs, subduction–accretion at continental-edge and AMCG intraplate magmatism, *Journal of South American Earth Sciences*, *29*(1), 105-127, doi:https://doi.org/10.1016/j.jsames.2009.08.004.

Reiss, M. C., J. D. Muirhead, A. S. Laizer, F. Link, E. O. Kazimoto, C. J. Ebinger, and G. Rümpker (2021), The Impact of Complex Volcanic Plumbing on the Nature of Seismicity in the Developing Magmatic Natron Rift, Tanzania, *Frontiers in Earth Science*, *8*, doi:10.3389/feart.2020.609805.

Sánchez, G., R. Recio, O. Marcuzzi, M. Moreno, M. Araujo, C. Navarro, J. C. Suárez, J. Havskov, and L. Ottemöller (2013), The Argentinean National Network of Seismic and Strong-Motion Stations, *Seismological Research Letters*, *84*(5), 729-736, doi:10.1785/0220120045.

Scholz, C. J. (1998), Earthquakes and friction laws, *Nature*, *391*, 37-42.

Schorlemmer, D., F. Euchner, P. Kästli, and J. Saul (2011), QuakeML: status of the XML-based seismological data exchange format, *2011*, *54*(1), 7, doi:10.4401/ag-4874.

Schurr, B., G. Asch, A. Rietbrock, R. Kind, M. Pardo, B. Heit, and T. Monfret (1999), Seismicity and average velocities beneath the Argentine Puna Plateau, *Geophysical Research Letters*, *26*(19), 3025-3028, doi:https://doi.org/10.1029/1999GL005385.

Schurr, B., G. Asch, A. Rietbrock, R. Trumbull, and C. Haberland (2003), Complex patterns of fluid and melt transport in the central Andean subduction zone revealed by attenuation tomography, *Earth and Planetary Science Letters*, *215*(1–2), 105-119, doi:http://dx.doi.org/10.1016/S0012-821X(03)00441-2.

Schurr, B., L. Ratschbacher, C. Sippl, R. Gloaguen, X. Yuan, and J. Mechie (2014), Seismotectonics of the Pamir, *Tectonics*, *33*(8), 1501-1518, doi:https://doi.org/10.1002/2014TC003576.

Schweitzer, J. (2001), HYPOSAT – An Enhanced Routine to Locate Seismic Events, *pure and applied geophysics*, *158*(1), 277-289, doi:10.1007/PL00001160.

Scott, C., R. Lohman, M. Pritchard, P. Alvarado, and G. Sánchez (2014), Andean earthquakes triggered by the 2010 Maule, Chile (Mw 8.8) earthquake: Comparisons of geodetic, seismic and geologic constraints, *Journal of South American Earth Sciences*, *50*, 27-39, doi:https://doi.org/10.1016/j.jsames.2013.12.001.

Seagren, E. G., M. McMillan, and L. M. Schoenbohm (2022), Tectonic Control on Drainage Evolution in Broken Forelands: Examples From NW Argentina, *Tectonics*, *41*(1), e2020TC006536, doi:https://doi.org/10.1029/2020TC006536.

Sibson, R. H. (1982), Fault zone models, heat flow, and the depth distribution of earthquakes in the continental crust of the United States, *Bulletin of the Seismological Society of America*, *72*(1), 151-163, doi:10.1785/bssa0720010151.

Sippl, C., et al. (2013), Geometry of the Pamir-Hindu Kush intermediate-depth earthquake zone from local seismic data, *Journal of Geophysical Research: Solid Earth*, *118*(4), 1438-1457, doi:https://doi.org/10.1002/jgrb.50128.

Sloan, R. A., J. A. Jackson, D. McKenzie, and K. Priestley (2011), Earthquake depth distributions in central Asia, and their relations with lithosphere thickness, shortening and extension, *Geophysical Journal International*, *185*(1), 1-29, doi:10.1111/j.1365-246X.2010.04882.x.

Smalley Jr., R., J. Pujol, M. Regnier, J. M. Chiu, J. L. Chatelain, B. Isacks, M. Araujo, and N. Puebla (1993), Basement seismicity beneath the Andean precordillera thin-skinned thrust belt and implications for crustal and lithospheric behavior, *Tectonics*, *12*(1), 63-76, doi:https://doi.org/10.1029/92TC01108.

Storchak, D. A., J. Schweitzer, and P. Bormann (2003), The IASPEI Standard Seismic Phase List, *Seismological Research Letters*, *74*(6), 761-772, doi:10.1785/gssrl.74.6.761.

Strecker, M. R., R. N. Alonso, B. Bookhagen, B. Carrapa, G. E. Hilley, E. R. Sobel, and M. H. Trauth (2007), Tectonics and Climate of the Southern Central Andes, *Annual Review of Earth and Planetary Sciences*, *35*(1), 747-787, doi:10.1146/annurev.earth.35.031306.140158.

Strecker, M. R., G. E. Hilley, B. Bookhagen, and E. R. Sobel (2012), Structural, Geomorphic, and Depositional Characteristics of Contiguous and Broken Foreland Basins: Examples from the Eastern Flanks of the Central Andes in Bolivia and NW Argentina, in *Tectonics of Sedimentary Basins*, edited, pp. 508-521, doi:10.1002/9781444347166.ch25.

Taboada, A., L. A. Rivera, A. Fuenzalida, A. Cisternas, H. Philip, H. Bijwaard, J. Olaya, and C. Rivera (2000), Geodynamics of the northern Andes: Subductions and intracontinental deformation (Colombia), *Tectonics*, *19*(5), 787-813, doi:https://doi.org/10.1029/2000TC900004.

Tassara, A., and A. Echaurren (2012), Anatomy of the Andean subduction zone: three-dimensional density model upgraded and compared against global-scale models, *Geophysical Journal International*, *189*(1), 161-168, doi:doi:10.1111/j.1365-246X.2012.05397.x.

Tongue, J. A., P. K. H. Maguire, and P. A. V. Young (1992), Seismicity distribution from temporary earthquake recording networks in Kenya, *Tectonophysics*, *204*(1-2), 71-79, doi:10.1016/0040-1951(92)90270-g.

Utsu, T., Y. Ogata, S. Ritsuko, and Matsu-ura (1995), The Centenary of the Omori Formula for a Decay Law of Aftershock Activity, *Journal of physics of the earth*, *43*, 1-33.

Valenzuela-Malebrán, C., S. Cesca, J. A. López-Comino, M. Zeckra, F. Krüger, and T. Dahm (2022), Source mechanisms and rupture processes of the Jujuy seismic nest, Chile-Argentina border, *Journal of South American Earth Sciences*, *117*, 103887, doi:https://doi.org/10.1016/j.jsames.2022.103887.

Vásquez, M., and U. Altenberger (2005), Mid-Cretaceous extension-related magmatism in the eastern Colombian Andes, *Journal of South American Earth Sciences*, *20*(3), 193-210, doi:https://doi.org/10.1016/j.jsames.2005.05.010.

Viramonte, J. G., S. M. Kay, R. Becchio, M. Escayola, and I. Novitski (1999), Cretaceous rift related magmatism in central-western South America, *Journal of South American Earth Sciences*, *12*(2), 109-121, doi:https://doi.org/10.1016/S0895-9811(99)00009-7.

Waldhauser, F., and W. L. Ellsworth (2000), A Double-difference Earthquake location algorithm: Method and application to the Northern Hayward Fault, California, *Bulletin of the Seismological Society of America*, *90*(6), 1353-1368, doi:10.1785/0120000006.

Weber, M., J. Tarney, P. Kempton, and R. Kent (2002), Crustal make-up of the Northern Andes: Evidence based on deep crustal xenolith suites, Mercaderes, SW Colombia, *Tectonophysics*, *345*, 49-82, doi:10.1016/S0040-1951(01)00206-2.

Weiss, J. R., et al. (2016), Isolating active orogenic wedge deformation in the southern Subandes of Bolivia, *Journal of Geophysical Research: Solid Earth*, *121*(8), 6192-6218, doi:10.1002/2016JB013145.

Weiss, J. R., G. Ito, B. A. Brooks, J.-A. Olive, J. H. Foster, and G. F. Moore (2018), Formation of the frontal zone of accretionary wedges, *Earth and Planetary Science Letters*, *495*, 87-100, doi:10.1016/j.epsl.2018.05.010.

Wessel, P., W. H. F. Smith, R. Scharroo, J. Luis, and F. Wobbe (2013), Generic Mapping Tools: Improved Version Released, *Eos, Transactions American Geophysical Union*, *94*(45), 409-410, doi:10.1002/2013EO450001.

Whitman, D. (1994), Moho geometry beneath the eastern margin of the Andes, northwest Argentina, and its implications to the effective elastic thickness of the Andean foreland, *J Geophys Res-Sol Ea*, *99*(B8), 15277-15289, doi:10.1029/94jb00342.

Whitman, D., B. L. Isacks, J. L. Chatelain, J. M. Chiu, and A. Perez (1992), Attentuation of high-frequency seismic-waves beneath the central Andean plateau, *J Geophys Res-Sol Ea*, *97*(B13), 19929-19947, doi:10.1029/92jb01748.

Willett, S. D. (1999), Orogeny and orography: The effects of erosion on the structure of mountain belts, *J Geophys Res-Sol Ea*, *104*(B12), 28957-28981, doi:Doi 10.1029/1999jb900248.

Wimpenny, S. (2022), Weak, Seismogenic Faults Inherited From Mesozoic Rifts Control Mountain Building in the Andean Foreland, *Geochemistry, Geophysics, Geosystems*, *23*, e2021GC010270, doi:10.1029/2021GC010270.

Wimpenny, S., A. Copley, C. Benavente, and E. Aguirre (2018), Extension and Dynamics of the Andes Inferred From the 2016 Parina (Huarichancara) Earthquake, *Journal of Geophysical Research: Solid Earth*, *123*(9), 8198-8228, doi:10.1029/2018jb015588.

Woessner, J., and S. Wiemer (2005), Assessing the Quality of Earthquake Catalogues: Estimating the Magnitude of Completeness and Its Uncertainty, *Bulletin of the Seismological Society of America*, *95*(2), 684-698, doi:10.1785/0120040007.

Yardley, B. W. D., and J. W. Valley (1997), The petrologic case for a dry lower crust, *Journal of Geophysical Research: Solid Earth*, *102*(B6), 12173-12185, doi:doi.org/10.1029/97JB00508.

Zeckra, M. (2020), Seismological and Seismotectonic Analysis of the Northwestern Argentine Central Andean Foreland, 120 pp, University of Potsdam, Potsdam, Germany.

Zeckra, M., and F. Kruger (2016), Seismic neTwoRk/Array in norThwEstern arGentina, edited, International Federation of Digital Seismograph Networks, doi:10.7914/SN/2S_2016.

Zoback, M. D., et al. (1987), New Evidence on the State of Stress of the San Andreas Fault System, *Science*, *238*(4830), 1105-1111, doi:doi:10.1126/science.238.4830.1105.

Zossi, M. M. (1979), Estudio de la actividad sismica de la Privincia de Tucuman, doctoral thesis, 125 pp, Universidad Nacional de Tucuman.